Measurement of the ^{160}Gd(p,n)^{160}Tb excitation function from 4 18 MeV, using a stacked foil technique

Ryan K. Chapman

Recommended Citation

Chapman, Ryan K., "Measurement of the ^{160}Gd(p,n)^{160}Tb excitation function from 4 18 MeV, using a stacked foil technique" (2020). *Theses and Dissertations*. 3595.
https://scholar.afit.edu/etd/3595

MEASUREMENT OF THE ^{160}Gd(p,n)^{160}Tb EXCITATION FUNCTION FROM 4-18 MeV, USING A STACKED FOIL TECHNIQUE

THESIS

Ryan K. Chapman, Major, USAF

AFIT-ENP-MS-20-M-088

DEPARTMENT OF THE AIR FORCE
AIR UNIVERSITY

AIR FORCE INSTITUTE OF TECHNOLOGY

Wright-Patterson Air Force Base, Ohio

MEASUREMENT OF THE ^{160}Gd(p,n)^{160}Tb EXCITATION FUNCTION FROM

4-18 MeV, USING A STACKED FOIL TECHNIQUE

THESIS

Presented to the Faculty

Department of Engineering Physics

Graduate School of Engineering and Management

Air Force Institute of Technology

Air University

Air Education and Training Command

in Partial Fulfillment of the Requirements for the

Degree of Master of Science

Ryan K. Chapman, BS

Major, USAF

March 2020

MEASUREMENT OF THE ^{160}Gd(p,n)^{160}Tb EXCITATION FUNCTION FROM

4-18 MeV, USING A STACKED FOIL TECHNIQUE

THESIS

Ryan K. Chapman, BS
Major, USAF

Committee Membership:

Maj James E. Bevins, Ph.D.
Chair

Dr. Abigail A. Bickley
Member

Dr. John W. McClory
Member

Dr. Narek Gharibyan
Member

Abstract

A stack of thin Gd, Ti, and Cu foils were irradiated with an 18 MeV proton beam at Lawrence-Berkeley National Laboratory's 88-Inch Cyclotron to investigate the ^{160}Gd(p,n)^{160}Tb nuclear reaction for post-detonation nuclear forensic applications. This experiment will improve knowledge of ^{160}Tb production rates, allowing ^{160}Tb to be efficiently created in a foil stack consisting of other proton induced isotopes for forensics applications. A set of 15 measured cross sections between 4-18 MeV for ^{160}Gd(p,n)^{160}Tb were obtained using a stacked foil technique. The foil stack consisted of one stainless steel, one iron, fifteen gadolinium, nine copper, and eight titanium foils. The stainless steel and iron foils were used to radiograph the beam spot size. Each Gd foil was encapsulated in Kapton tape prior to irradiation to minimize oxidation. The copper, ^{62}Cu(p,n)^{62}Zn and ^{65}Cu(p,n)^{65}Zn, and titanium, ^{48}Ti(p,n)^{48}V and ^{nat}Ti(p,x)^{46}Sc, foils served as monitor foils to determine the proton fluence throughout the stack. Variance minimization using a MCNP6.2 model was used to improve the reliability of the cross-section measurements by reducing the uncertainties in proton energy and fluence by varying the density and incident beam energy within the uncertainty in the measurement of each. The measured cross section of the ^{160}Gd(p,n)^{160}Tb generally follows the shape predicted by TENDL-2019, but the cross sections obtained in this work indicate approximately a 20% increase in the maximum cross section. Additionally, other ^{nat}Gd(p,x) reactions were created through the irradiation, providing experimental measurements of ^{154}Gd(p,2n)^{153}Tb, ^{nat}Gd(p,x)^{152}Eu, ^{nat}Gd(p,x)^{154}Tb, ^{nat}Gd(p,x)^{155}Tb, ^{nat}Gd(p,x)^{156}Tb, ^{nat}Gd(p,x)^{154}Eu, ^{nat}Gd(p,x)^{157}Eu, and ^{nat}Gd(p,x)^{159}Gd reactions.

Acknowledgements

Thank you to my family for their support, my peers who helped me through this Masters program, and most of all my advisor, James, for answering countless questions, reviewing thousands of lines of choppy code, and instilling confidence in me as a Nuclear Engineer.

Ryan K. Chapman

Table of Contents

List of Figures

List of Tables

MEASUREMENT OF THE ^{160}Gd(p,n)^{160}Tb EXCITATION FUNCTION FROM 4-18 MeV, USING A STACKED FOIL TECHNIQUE

I. Introduction

Nuclear data are the foundation for all radiation transport software, and incorrect nuclear data can drastically affect the results obtained from the software. However, in many cases, especially for charged particle reactions, experimental nuclear data are limited and not well characterized thereby limiting their usefulness as an input into radiation transport simulations. To address this need, the Department of Energy's (DOE) Nuclear Science Advisory Committee Isotope (NSACI) has the mission to "identify and prioritize the most compelling opportunities for the DOE Isotope Program to pursue over the next decade and articulate their impact [5]." NSACI teamed with academia to host the Nuclear Data Needs and Capabilities for Applications workshop in 2015 [5]. This workshop was broad in nature, focusing on all potential data needs. After these broad needs were identified, a subsequent workshop was held in 2016 to focus and prioritize these needs by the DOE at the Nuclear Data Needs and Capabilities for Basic Science workshop [6].

From these workshops, a prioritized plan to study nuclear data was developed. These workshops have maintained a focus for modern nuclear data collection primarily in the fields of medical isotope production and nuclear reactors. This trend continues up to 2019, most recently at the Workshop for Applied Nuclear Data Activities [7]. However, defense needs and applications have been generally under-represented both

in terms of workshop attendance and data needs prioritization.

The ^{160}Gd(p,n)^{160}Tb reaction explored in this thesis is an example of a defense application that was not considered or prioritized through the primary data collection efforts [6,7]. This reaction does not directly contribute in the areas of nuclear reactors or nuclear medicine, rather it is an important reaction in the field of technical nuclear forensics used in post-detonation debris analysis to understand the characteristics of a detonated nuclear weapon.

Nuclear forensics' data needs are not as widely broadcasted as nuclear medicine and reactors due to the size of the field and financial incentives. Additionally, there can be classification issues with how the nuclear data are used for forensic purposes. However an unclassified memo from Lawrence Livermore National Laboratory (LLNL) details how the ratio of ^{161}Tb:^{160}Tb allows for background correction of ^{161}Tb, an important fission product for fission split determination [8]. As such, ^{160}Tb is routinely included in surrogate debris samples utilized in baselining post-detonation laboratory analysis capabilities. Improving the ^{160}Gd(p,n)^{160}Tb cross-section helps sample production efforts in support of this forensic mission.

1.1 Background

Post-detonation nuclear forensic experts practice their craft like any other technician does. In order for these technicians to train, post-detonation surrogate samples are formed, consisting of the same isotopes that would be present in the environment following a real nuclear test. Creation of these test samples is done through irradiating stable isotopes with proton or alpha particles to create the unique radioisotopes observed after a nuclear explosion. One of these radioisotopes observed in the post-detonation sample would be ^{160}Tb produced by neutron capture of ^{159}Tb found naturally in the soil. ^{160}Tb can be produced through a variety of different methods,

such as neutron capture on ^{159}Tb, or (d,2n) on ^{160}Gd. However, (p,n) is chosen due to other post-detonation surrogate samples' reliance on proton irradiation. Using a (p,n) reaction, ^{160}Tb can be created in conjunction with a stack of post-detonation target foils for producing other isotopes of interest.

Understanding the ^{160}Tb production mechanisms can reduce the time and cost associated with producing these surrogate post-detonation samples. Additionally, with well understood production cross sections, a single post-detonation sample can be created by arranging a stack of different isotopic foils and modeling the beam's energy degradation; thus, optimally aligning the isotopes needed at the corresponding energies and allowing for a single irradiation to create the multiple isotopes for a sample. Finally, it is important to understand that the ^{160}Gd(p,n)^{160}Tb excitation function, and most other proton or charged particle induced reactions, are much less known compared to their neutron counterparts. This thesis experiment will help lift the shroud on charged particle interactions, feeding the existing theoretical models with data to update the predictions.

There are two other experimental measurements of the ^{160}Gd(p,n)^{160}Tb reaction, the first of which occurred in 1973. Birattari et al., measured the ^{160}Gd(p,n)^{160}Tb in the 5-45 MeV energy range at a cyclotron located in Milan, Italy [9]. Due to this high range of incident proton energies, only seven measurements were made in the 4-18 MeV range where the production of ^{160}Tb is maximized. In addition to providing new, higher fidelity data, this research provides more measurements, 15, in the 4-18 MeV range. A detailed description of Birattari's experiment is provided in Section 2.6. The second experiment, led by Vermeulen in 2012, examined irradiating ^{nat}Gd with protons with initial energies of 66 MeV. The high initial energy, combined with Vermeulen's main goal of measuring ^{152}Tb and ^{155}Tb, led to only two ^{160}Tb measurements in the energy range of this experiment [10]. Unfortunately, one of the

two points is reported with over 100% uncertainty, on both EXFOR and in the journal paper [10, 11].

The TALYS-based evaluated nuclear data library (TENDL) is a nuclear-data library based upon the TALYS nuclear model [12]. TENDL contains model-based evaluations for seven different incident particles, for isotopes with half-lives longer than a sec, and energies up to 200 MeV [13]. Experimental measurements feed into TENDL in the form of better TAYLS parameters. Updates are frequently published with the most recent being TENDL-2019, the tenth overall update to this model-based evaluated data library. TENDL predicts a peak of the ^{160}Gd(p,n)^{160}Tb excitation at 7 MeV, as shown in Figure 1.1.

The Proton Activation Data File (PADF) was composed to satisfy growing needs in nuclear data at intermediate energies. It contains calculated and evaluated excitation functions of nuclear reactions for the target nuclei at proton energies up to 150 MeV. Data are available in the PADF for stable and unstable target nuclei with half-life more than one sec [14]. Data for the PADF were obtained using the TALYS code, the ALICE/ASH code, and the existing experimental data [14].

Figure 1.1 shows a comparison between Birattari's and Vermeulen's experimental measurements and TENDL's theoretical predictions. Discrepancies exist between the slope in the 4-8 MeV range, where there are two, largely spaced experimental points, and at the higher energies, larger cross-section predicted by TENDL, versus the smaller cross-section measured by Birattari. Results of this thesis experiment will add three data points in the 4-8 MeV range, along with six data points above 12 MeV to assist in understanding of discrepancies between TENDL and the previous experimental data.
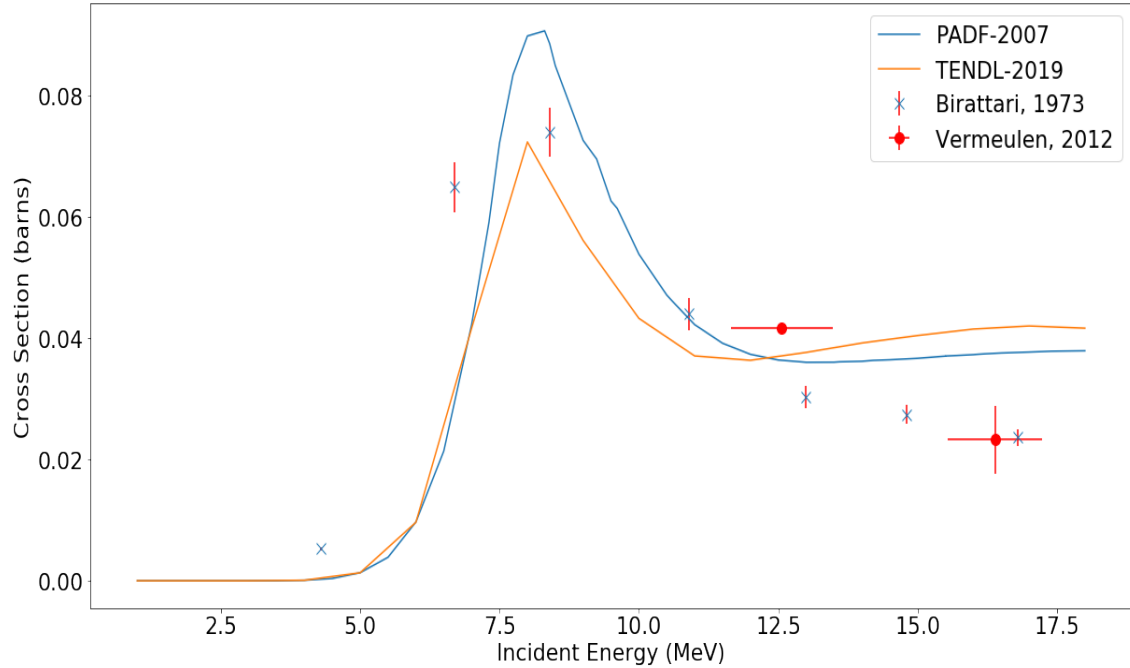
Figure 1.1. Comparison of TENDL to existing experimental data for the ^{160}Gd(p,n)^{160}Tb excitation function [9, 10, 13, 14].

1.2 Problem Statement

Nuclear data, the fundamental input to radiation transport software, are incomplete with many isotopes lacking experimental cross-section measurements. The ratio of ^{161}Tb:^{160}Tb is an important measurement for the nuclear forensic analysis of post-detonation debris. An improved measurement of the ^{160}Gd(p,n)^{160}Tb reaction cross section enhances the ability to produce post-detonation surrogate samples more efficiently and cost-effectively to enable training of forensic scientists and establish realistic analysis capabilities.

To measure the ^{160}Gd(p,n)^{160}Tb reaction cross section, several objectives and sub-objectives were used to segment the work into small, obtainable goals:

1. Design the ^{160}Gd(p,n) experiment.

    (a) Develop a MCNP6.2 [15] model of the experiment to model proton energy

loss through the foil stack.

    (b) Iterate model inputs to determine optimum order of Gd, Ti, and Cu foils.

    (c) Obtain the distribution of proton energies in each foil.

2. Irradiate the foil stack, based upon the model, at Lawerence Berkeley National Laboratory's (LBNL) 88-Inch cyclotron.

3. Perform high purity germanium (HPGe) gamma spectrometry measurements of activated foils.

    (a) Obtain energy and efficiency calibrations on each HPGe used.

    (b) Measure induced activity for the reactions of interest in the gadolinium and monitor reaction foils.

4. Calculate the ^{160}Gd(p,n)^{160}Tb reaction cross section.

    (a) Determine T_0 activity for monitor foil reactions.

    (b) Determine proton beam energy and current in each foil using a variance minimization technique.

1.3 Methodology

To minimize the time required to irradiate each of the 15 Gd foils at different energies, a stack of foils containing Gd, Ti, and Cu were used. As the proton beam travels through the foil stack, the distribution of proton energies broadens due to charged particle interactions with each of the foils. The result of this interaction is that a single irradiation can expose each of the 15 Gd foils at different energies and cover a broad energy range. However, the 15 Gd foils' stopping power will not lower the beam energy on their own from 18 to 4 MeV. Ti and Cu foils were interlaced in

6

the beam stack to reduce the energy of the beam across the foil stack to cover the energy range of interest.

The Ti and Cu foils also played another critical role in the foil stack. They serve as monitor foils, because the ^{nat}Ti(p,x)^{48}V, ^{nat}Ti(p,x)^{46}Sc, and ^{nat}Cu(p,n)^{65}Zn reaction cross-sections are well-known and characterized by multiple previous experimental measurements [3]. Measuring the activity of these reactions gives information into the actual beam energy and current hitting these foils. These monitor data are also used to account for the foil to foil current drop [16].

The dimensions and weight of all the foils (monitor and Gd) were categorized through high precision calipers, micrometers, and scales. However, each Gd foil was encased in Kapton tape, which has a claimed thickness of 10 microns from the manu- facturer but could not be directly measured. Since the uncertainty in the areal density (density multiplied by thickness) of this tape was unknown (largely because the ad- hesive composition is unknown), an iteration of the Kapton and adhesive densities in the MCNP6 model was performed to correct for uncertainties in this measurement. This process is described in Section 2.5.2.

The current information and induced reaction rates are then used to calculate the ^{160}Gd(p,n)^{160}Tb reaction cross section. Systematic and statistical uncertainty are propagated throughout to determine the uncertainty in the total cross section calculated. The beam energy range covered by each foil is determined using the experimentally-calibrated MCNP6 model.

1.4   Assumptions and Limitations

The most significant limitation in this experiment was oxidation of the Gd foils when exposed to air, potentially leading to the loss of mass and activation products causing an under-calculation of the reaction cross-section, along with contamination.

This limitaiton led to encapsulating each Gd foil in Kapton tape. Each Gd foil was taken directly from its argon-filled packaging, weighed, measured with a micrometer, and then encapsulated with the Kapton tape. Once encapsulated, the foils' length and width were measured to determine the density of each foil.

The encapsulation came with many side-effects, the first of which was modeling 30 pieces of tape in the MCNP model. To do this, the Kapton material was extracted from the PNNL material guide, while the adhesive was modeled as natural Si [17]. Since the Kapton and adhesive densities and thicknesses were not well characterized, the variance minimization method described in Section 1.3 was implemented. This implicitly assumes that the monitor reactions cross-sections are well-known and any variance is due to Kapton and adhesive areal density or stopping power inaccuracies. This is a common assumption in the literature [16] [18] and appropriate for this experiment as it ties the accuracy of the measurement to the accuracy of the monitor foil cross-sections used.

Another limitation was in the design of the foil irradiation configuration. Initially, a high energy and low energy runs were planned, irradiating eight Gd foils in each run. This would have provided 16 data points and would have reduced the uncertainty in energy space of each data point since the energy uncertainty increases as the beam propagates through more material. Due to scheduling limitations, a single irradiation of 15 foils was used instead. With a single run and thicker foil stack, the spread of energies covered by each foil increase as a function of its position in the stack. This results in higher energy uncertainty for the Gd foils further along the foil stack in comparision to performing two irradiations with different incident energies.

1.5 Significant Research Contributions

1. *Improved the production of post-detonation debris for the nuclear forensics field:* Through better understanding of the ^{160}Gd(p,n)^{160}Tb cross-section, post-detonation surrogate debris samples can be produced more efficiently, reducing the amount of time required to create these samples and allowing multiple isotopes to be created by the same charged particle irradiation through an optimized foil stack.

2. *Provided data to improve existing nuclear data models:* Models, such as TENDL, are constantly being updated. The ^{160}Gd(p,n)^{160}Tb cross-section predicted by TENDL changed by 5% in some energy regions from TENDL-2017 to TENDL-2019. These models benefit greatly from charged particle experimental measurements like this one.

3. *Performed first ever experimental measurements for seven other nuclear reactions:* Gd contains seven different naturally occurring isotopes, all which underwent various nuclear reactions when bombarded by protons. Future work will analyze the cross-sections of seven of these reactions.

II. Literature Review

This literature review steps through the background knowledge required to under-stand the basic physics and concepts related to this work. First, the fundamentals of how a cyclotron, the source of the proton beam, operates is described. Next, charged particle interactions are detailed, which serve as the basis for understanding how the proton beam degrades as it progresses through the foil stack. Then, nuclear reactions are highlighted to explain how and when the ^{160}Gd(p,n)^{160}Tb reaction occurs. An overview of gamma spectroscopy is then provided to link the observable data to cross-sections. This is followed by a description of the stacked foil technique and an explanation of how monitor reactions can be used to determine proton fluence in a foil stack.

This information is then used to describe and analyze previous experiments per-formed on the ^{160}Gd(p,n)^{160}Tb from 1973 and 2012 [9, 10]. Finally, this chapter closes by outlining a variance minimization technique to minimize uncertainty in the experiment and better quantify the measured excitation functions.

2.1   Cyclotron Overview

The proton beam used in this experiment is generated by a cyclotron. A cyclotron operates by accelerating a charged particle in a spiral motion. As the particle spins outward, it is accelerated by passing through two connected "D's." Each D has an al-ternating electric field which aligns with the polarity of the charged particle, increases its energy as it spirals out.

The LBNL 88-Inch Cyclotron has a maximum current on the order of 10 mi-croamperes, with a maximum beam power of 2 kW. The beam can be extracted from the machine for use in experiments in 7 separate "caves" [19]. Figure 2.1 shows the

path from the cyclotron to each of the seven caves. Cave 02 was utilized for this experiment.
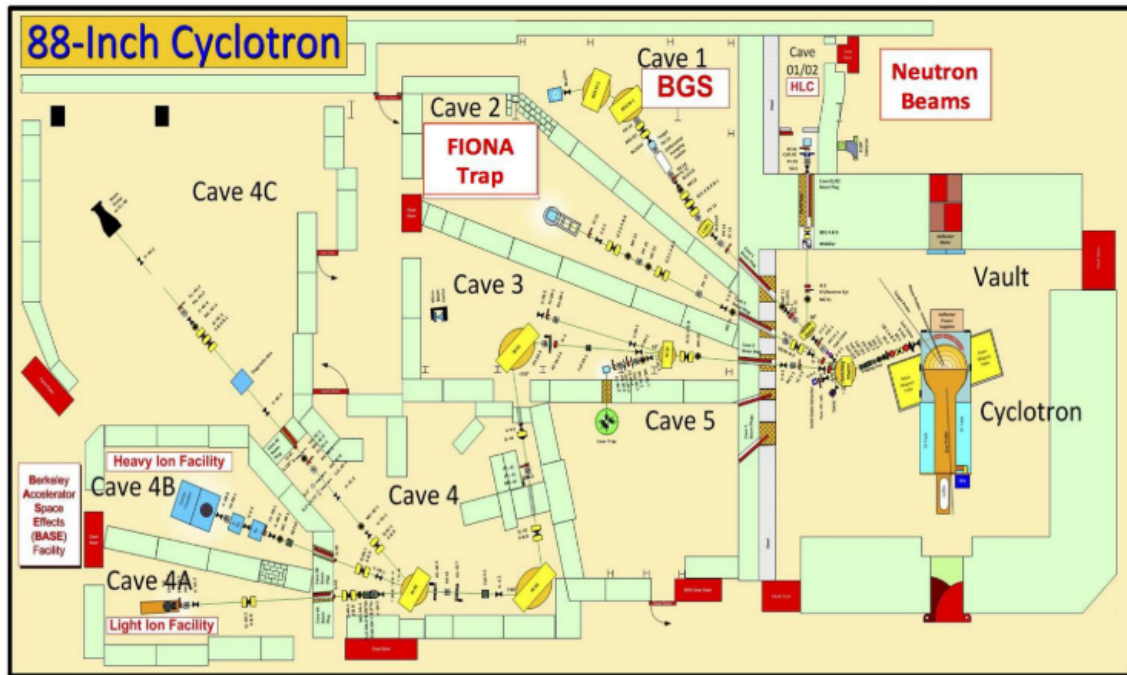
Figure 2.1. Schematic of LBNL's 88-Inch Cyclotron displaying each of the beam lines and experimental caves [19].

.

2.2 Charged Particle Interactions

The basis for understanding the stacked foil technique mentioned in the title of this thesis requires knowledge of how charged particles interact with matter. At the simplest level, the proton beam produced by LBNL's 88-Inch Cyclotron penetrates the foil stack and loses energy through interaction with each successive foil resulting in a lower energy for each subsequent foil in the stack. The continuous beam is comprised of trillions of protons, which all leave the cyclotron and enter Cave 0 at 18 MeV with an approximately 2% energy width due to the multi-turn extraction [20]. However, the stochastic nature of charged particle interactions results in a decreased beam intensity and broadening of in energy and space. To understand the physics at

hand, several terms will be introduced and described in detail.

It is best to look at charged particle interactions through the lens of the MCNP6.2 model as this model was used in this work. MCNP6.2 calculates energy loss through the continuous energy loss model and accounts for range straggling and angular scatter. For continuous energy loss, protons lose energy from one of three different energy loss channels, depending on their incident energy. The first region, modeled by Bethe's theory, is valid for energies above 5.24 MeV and is given as

$$-\frac{1}{\rho}\frac{dE}{dx} = \frac{4\pi r_e^2 mc^2}{\beta^2}\frac{1}{u}\frac{\Sigma_i Z_i f_i}{\Sigma_i A_i f_i}z^2 L(\beta), \qquad (2.1)$$

where ρ is the material density [g/cm^3], $\frac{dE}{dx}$ is stopping power [MeV/cm], r_e is the radius of an electron [cm], m is the particle mass [MeV], c is the speed of light [m/s], β is the ratio of particle velocity to the speed of light, u is the atomic mass unit, Z_i is the atomic number for each element, f_i is the atom fraction for each element, A_i is the atomic weight for each element, and z is the charge of the charged particle [1]. $L(\beta)$ is given by

$$L(\beta) = \frac{1}{2}ln(\frac{2mc^2\beta W_m}{1-\beta^2}) - \beta^2 - \frac{\Sigma_i Z_i f_i ln(I_i)}{\Sigma_i Z_i f_i} - \Sigma_i\frac{C_i f_i}{Z_i} - \frac{\delta(\beta, z, I)}{2}, \qquad (2.2)$$

where W_m is the max possible energy transfer in an inelastic Coulomb collision with an atomic electron [eV], I is the mean excitation energy [eV], C_i is the shell or subshell correction, δ is the density-effect correction [1], and the iterator, i represents these properties for each element interacting with the charged particle.

The second region for energy loss occurs when the incident particle is below 1.31 MeV. Here the particles are treated as traveling through a gas of free electrons that generate a stationary electric field [1]. Particles traveling in the medium are assumed

12

to be point charges with constant velocity that experience Coulombic resistance from the electron gas. The third region occurs in between 1.31 and 5.24 MeV where an interpolation between the two models is performed.

In addition to continuous energy loss, MCNP6.2 also handles another phenomenon of charged particle energy loss, energy straggling. Energy straggling is the statistical distribution of charged particles about a mean range after continuous energy loss in a medium, illustrated in Figure 2.2 [1, 21].
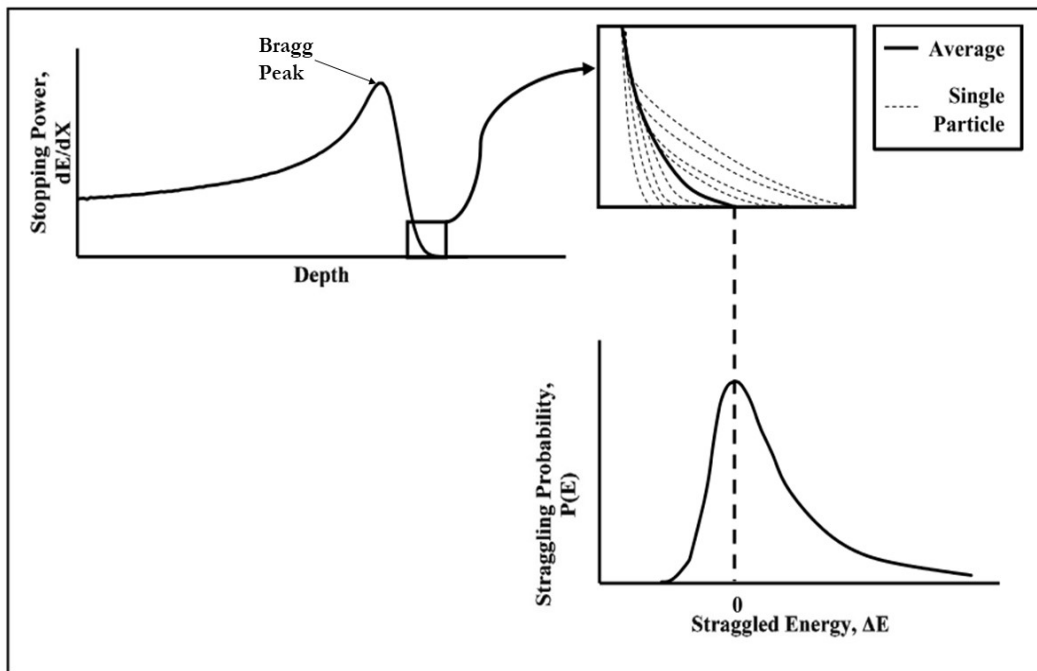
Figure 2.2. Depiction of stopping power, straggling, and the Bragg peak [1].

When discussing the range of charged particles in matter, the "range" is traditionally the average distance traveled by a species of charged particle in a given medium. This location is referred to as the Bragg Peak and is shown in Figure 2.2. In reality, due to the random nature of particle interactions, each individual charged particle will experience a different range in the medium, as shown in Figure 2.2. MCNP6.2 calculates straggling from piece-wise approximation of the Vavilov distribution to determine the amount of straggling that occurs [1]. The Vavilov distribution is rep-

resented by a probability density function, also shown in Figure 2.2. This function gives the probability that a charged particle traversing a path length will be affected by an energy loss from multiple single scatters. MCNP6.2 begins by calculating the continuous energy loss for a particle and then calculates straggling. The straggled energy is stored temporarily, then subtracted from the final estimated particle energy. Figure 2.3 shows this sampling occurring with ΔE_n representing the straggled energy.

Angular scattering in MCNP6.2 is modeled according to a modified version of the multiple scattering theory developed by Moliere, called the FNAL2 model [1]. This model returns a scattering angle to the main transport routine. Figure 2.3 depicts the angular scattering model. At the end of each step through the medium, the particle loses some energy ΔE that is a combination of continuous energy loss and energy straggling. Next, the total angular deflection (from scattering) over a step is calculated. Finally the particle's direction and position vectors are updated. Each of the trillions of protons inside the cyclotron's beam interact with the atoms inside each of the foils according to the above models and equations.

2.3   Nuclear Reactions

Now that an understanding of the proton beam, along with how the individual protons within the beam can interact with matter, is established, there is another form of proton interaction within the foils that must be examined – nuclear reactions. This is the type of interaction that this thesis experiment is measuring, the probability that a proton at a given energy will be absorbed by a ^{160}Gd nucleus ejecting a neutron and producing ^{160}Tb. A typical nuclear reaction is often written as

$$a + X \rightarrow Y + b, \tag{2.3}$$

14

n^{th} Step $(n+1)^{\text{th}}$ Step $(n+2)^{\text{th}}$ Step

θ_2

$E_f = E_{(n+2)}$

E_0

θ_1

θ_3

$E_n = E_0 - \Delta E_n$ $E_{(n+1)} = E_n - \Delta E_{(n+1)}$ $E_{(n+2)} = E_{(n+1)} - \Delta E_{(n+2)}$

Δx_n $\Delta x_{(n+1)}$ $\Delta x_{(n+2)}$
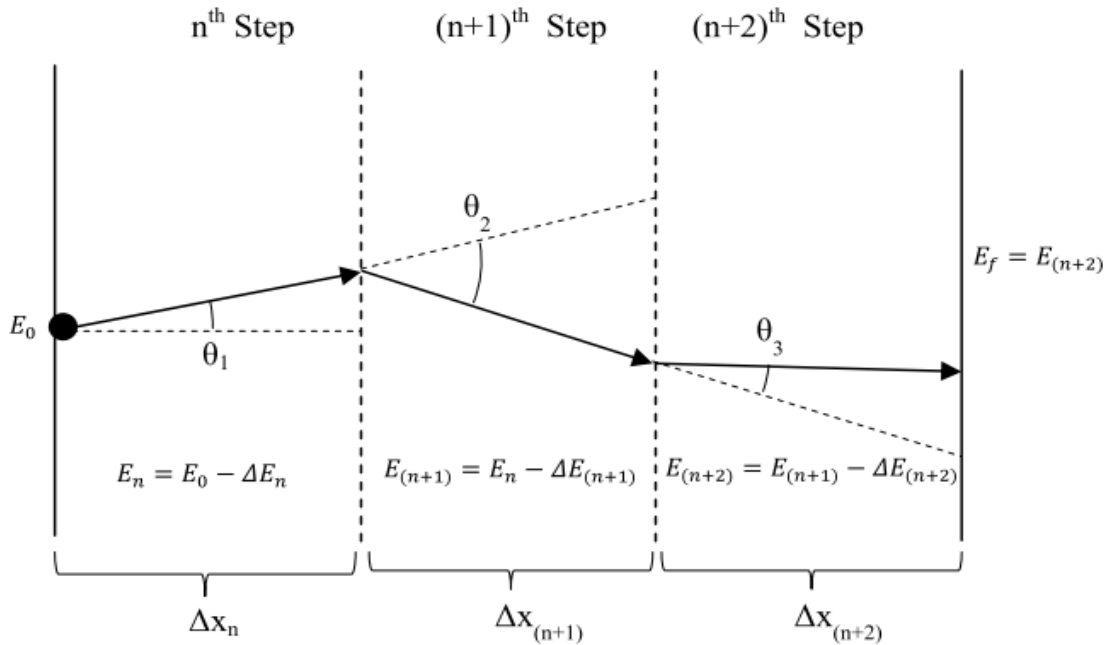
Figure 2.3. Angular scattering as calculated in MCNP6.2 [1].

where a is the accelerated particle, X is the target atom, Y is the reaction atom, and b is the ejected particle [22]. These reactions can proceed via direct and compound reactions. The type of reaction affects the energies and angles of the secondary particles emitted.

A direct reaction occurs when nucleons are directly "knocked" out of the target by the projectile, such as an incoming proton ejecting a neutron from the target, thereby removing one nucleon from the target X to form Y. Direct reactions are more likely to occur when the incident energy of in projectile particle is high (15-20 MeV). This is because its wavelength is shorter, causing the particle to have a higher probability of interacting with individual nucleons versus the nucleus as a whole [22].

At lower energies (1-5 MeV), a compound reaction is more probable. Equation 2.4 shows the general form of compound nuclear reactions. Here the inbound particle interacts with the entire nucleus, causing a compound nucleus to be formed. The energy from the inbound particle is transferred to the nucleons inside the nucleus,

15

often causing a particle to be ejected. The energy range of this experiment causes the ^{160}Gd(p,n)^{160}Tb reaction to transition from a pure compound reaction at lower energies to a mix of direct and compound reactions at higher energies.

$$a + X \rightarrow C^* \rightarrow Y + b \tag{2.4}$$

^{160}Gd(p,n)^{160}Tb is an example of a transfer reaction.

For any nuclear reaction to occur, a threshold energy must be reached by the projectile impacting an atom and is given by

$$T_{th} = (-Q)\frac{m_y + m_b}{m_y + m_b - m_a}, \tag{2.5}$$

where m is the mass of the inbound nuclide, ejected nuclide, or resultant atom, Q is defined as the initial rest mass energy minus the final rest mass energy for the nuclear reaction. Note, it is assumed the angle of the incident particle is $0°$. The threshold energy for the ^{160}Gd(p,n)^{160}Tb reaction is 893.4 *1.0* keV, while the Q-value is -887.8 *1.0* keV [23]. The negative Q-value means this reaction is endothermic and requires additional energy to occur. This required energy comes from the kinetic energy of the projectile (a proton in the case of this work).

2.4   Gamma Spectroscopy

To measure radioactive reaction products for determining the frequency of the associated nuclear reaction occurred, a detection technique known as gamma spectroscopy is used. Gamma spectroscopy refers to measuring gammas rays of distinct energy from a decaying nucleus to determine the activity of a material, relatable to the number of radioactive atoms. Gamma spectrometry is applying the spectroscopy on a particular detector.

The ^{160}Tb created by the ^{160}Gd(p,n)^{160}Tb reaction has a half life of 72.3 days [23]. As the ^{160}Tb β^- decays to ^{160}Dy, it is left in an excited state. The ^{160}Dy nucleus releases gamma rays to reduce its energy to a more stable level, typically the ground state of the nucleus. A High Purity Germanium (HPGe) detector is used to measure these gamma rays by placing the activated material near the detector in a shielded container to minimize background radiation.

One reason a HPGe detector was used for gamma spectrometry in this experiment is its superior energy resolution. Energy resolution, as the name suggests, is the parameter in which a detector can resolve a given energy. Energy resolution is defined by the full width half maximum (FWHM) of a given peak divided by location of a peak's centroid.

Another key characteristic for gamma spectrometry is the efficiency, which allows the amount of detected radiation to be related to the number of radioactive atoms in the sample. Knoll defines efficiency as [2]

$$\epsilon = \frac{number\,of\,pulses\,recorded}{number\,of\,radiation\,emitted\,by\,source}. \tag{2.6}$$

HPGe efficiencies are a function of the incident gamma energy. To relate detector counts to an activity, efficiency at each measured energy must be quantified. This is done by using an empirical curve fit, along with well characterized calibration sources, to fit an efficiency curve to a given detector. This process is described in Chapter 3.

Another factor impacting the relationship between what the detector measures and the activity of the item placed in the detector is dead time. Dead time is defined as the minimum amount of time needed by a detector to separate two events [2]. Dead time losses become severe when high counting rates are encountered, which can be the case directly after or close to irradiation if the sample activity is too high. To mitigate detector dead time, one can increase the distance from the source to the

detector, to lower the amount of radiation observed by the detector by decreasing the geometric efficiency.

All detectors also experience background radiation that can contaminate the data collected. HPGe detectors often use shielding to mitigate the amount of cosmic-ray background events which are recorded by the detector [2]. Even with shielding, there is still a background contribution, largely from radioactive contamination of shielding material [2]. These background contributions, or noise, scale with counting time; however, they can be overcome by the energy resolution of the detector. Figure 2.4 shows the effect of fine versus coarse energy resolution and the ability to distinguish signal from background noise with each.

There are several HPGe detector characteristics linking the activity of an irradiated foil to the amount of nuclear reactions that occurred from the proton irradiation. Understanding each of the factors draws a link between measurements from the HPGe detector and the observed reaction rate.

2.5   Stacked Foil Technique

A stacked foil technique was chosen for this experiment to measure the cross-section of the ^{160}Gd(p,n)^{160}Tb at multiple energies with a single irradiation [16]. A stacked foil technique involves aligning a series of target, degrader, and monitor foils to measure reaction data at different energy points than the incident beam energy. Modeling is then used to quantify the beam degradation through the stack to capture the distribution of proton energies impacting each foil [20, 24].

Without a stacked foil technique, each Gd foil would have to be irradiated independently at a desired energy. To quantify the time savings of using the stacked foil technique, consider the time it took for a single proton beam energy tune, 6 hours, along with the amount of foils irradiated, 15. Without using the stacked foil tech-
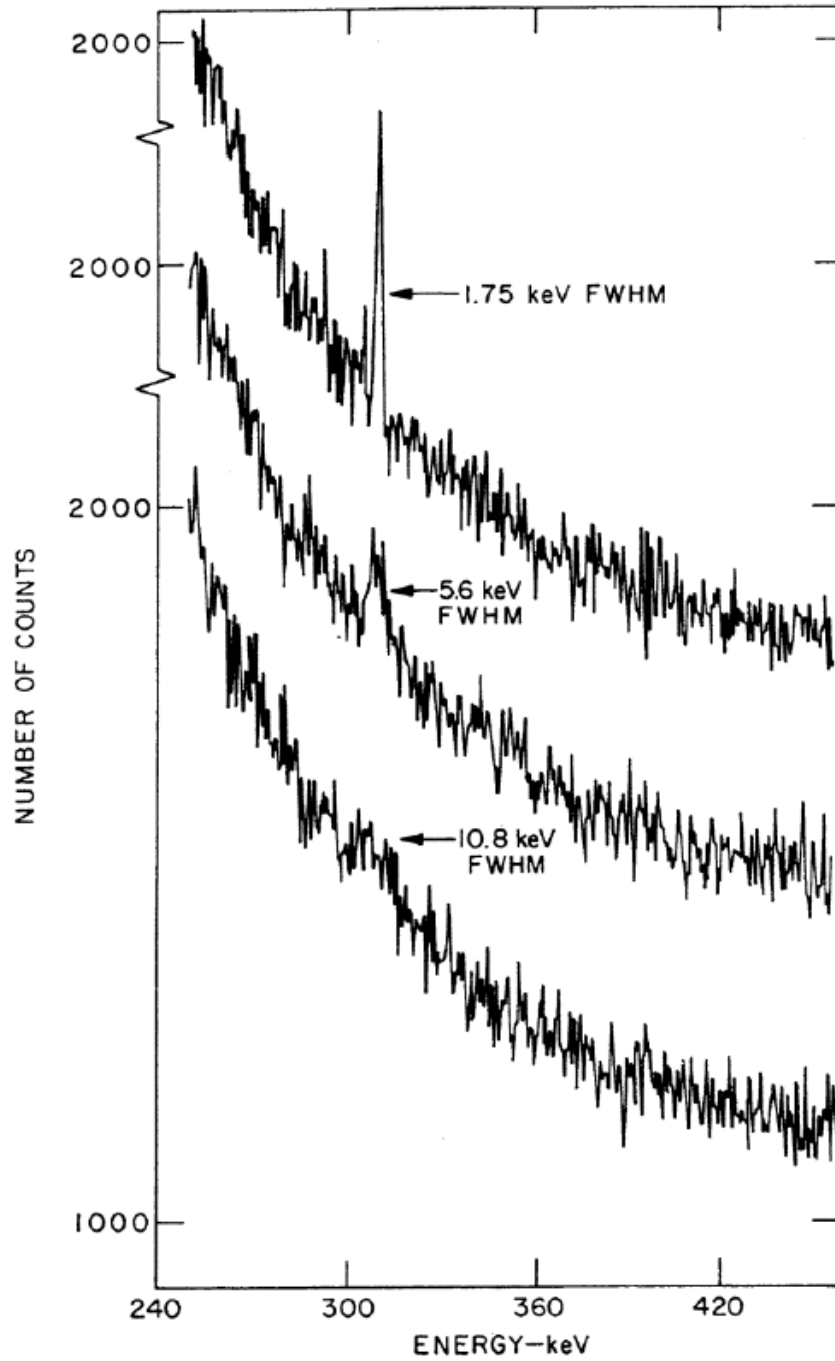
Figure 2.4. Comparison of Signal:Noise based on various detector energy resolutions.

nique, 90 hours of beam time, along with 90 min of irradiation time per Gd foil, would be required. Using the stacked foil technique saved over 100 hours of beam tuning and irradiation time.

19

When designing a foil stack, there is a delicate balance of target, degrader, and monitor foils. The degrader foils are designed to lower the energy of the beam as it progresses through the foil stack. The target foils used in this experiment are 10 microns thick, which is not enough to significantly degrade the beam. Monitor foils, discussed in the next section in more detail, give information about the proton current at different points inside the foil stack.

Another complicating factor is the random nature of charged particle transport contributing to uncertainty in energy incident on each foil. If the foil stack has too many foils, the energy uncertainty can become significant. This experiment had a relatively narrow energy range of 4-18 MeV, compared to other experiments which have an energy drop of up to 40 MeV [16,18,24]. Due to the 4-18 MeV range, monitor foils also functioned as degrader foils.

2.5.1 Monitor Reactions

Interlaced within the foil stack are several Ti and Cu foils, which act both as beam degraders and as monitor foils [18]. Monitor reactions, specifically the ^{nat}Ti(p,x)^{48}V, ^{nat}Ti(p,x)^{46}Sc, and ^{nat}Cu(p,x)^{65}Zn reactions, are all well studied and commonly used in stacked foil experiments [3,16,18,20,24]. Figures 2.5, 2.6, and 2.7 show the accepted evaluated cross section and experimental data for these monitor reactions. Using these monitor foil reactions, proton beam fluence, in units of nanonanoampere hours (nAh), can be determined by

$$I\Delta t = \frac{A_0 \Delta t}{\rho \Delta r (1 - e^{-\lambda \Delta t}) \int \sigma(E) \frac{d\phi}{dE} dE} \tag{2.7}$$

where A_0 is the experimentally measured T_0 activity of the monitor foils [Bqs] from Equation 3.6, Δt is the irradiation time [sec], $\rho \Delta r$ is the areal density of the monitor foil [$\frac{\#}{cm^2}$], λ is the decay constant in [sec] of the monitor foil reaction product, $\sigma(E)$

20

is the IAEA recommended cross section [cm^2] at energy E, and $\frac{d\phi}{dE}$ is the differential proton fluence [3, 16].
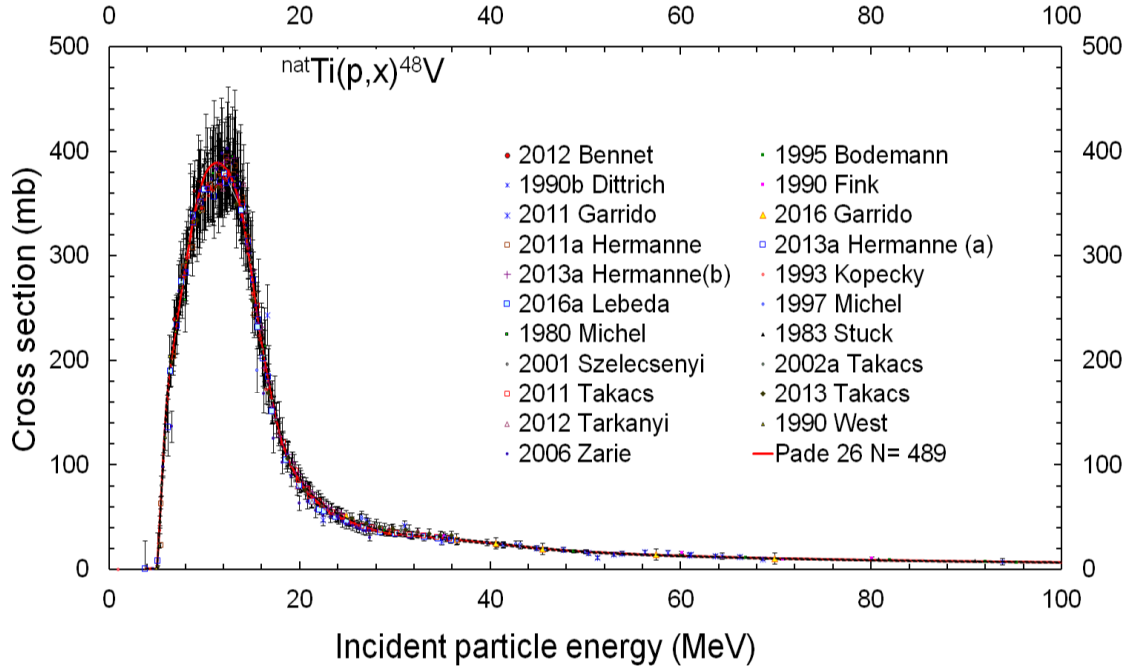
Figure 2.5. IAEA accepted cross-section data for the ^{nat}Ti(p,x)^{48}V reaction [3].

Insight into the proton energy at various points within the foil stack can be achieved by spacing monitor foils throughout the stack and measuring the number of reactions that occurred using gamma ray spectrometry as described in Section 2.4.

2.5.2 Proton Current Variance Minimization

To reduce the uncertainty in proton beam fluence and proton energy, a variance minimization technique described by Voyles and Graves is used [16, 18]. The method is based upon the assumption that monitor reaction cross-sections and MCNP6.2-modeled energy distributions, though not necessarily the mean energy, are both accurate. Therefore, a disagreement in the observed proton fluences is rooted in incorrectly characterized stopping power in simulations, uncertainty in the incident beam energy, or a systematic error in the areal densities of the stack components. The

21

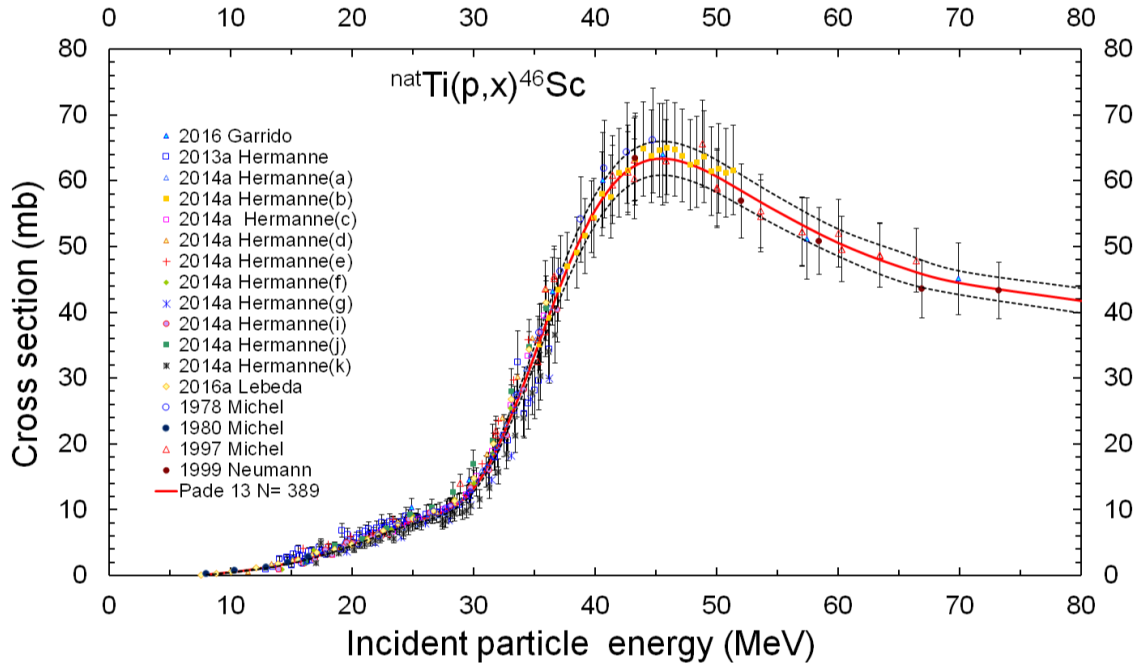**Figure 2.6. IAEA accepted cross-section data for the ^{nat}Ti(p,x)^{46}Sc reaction [3].**
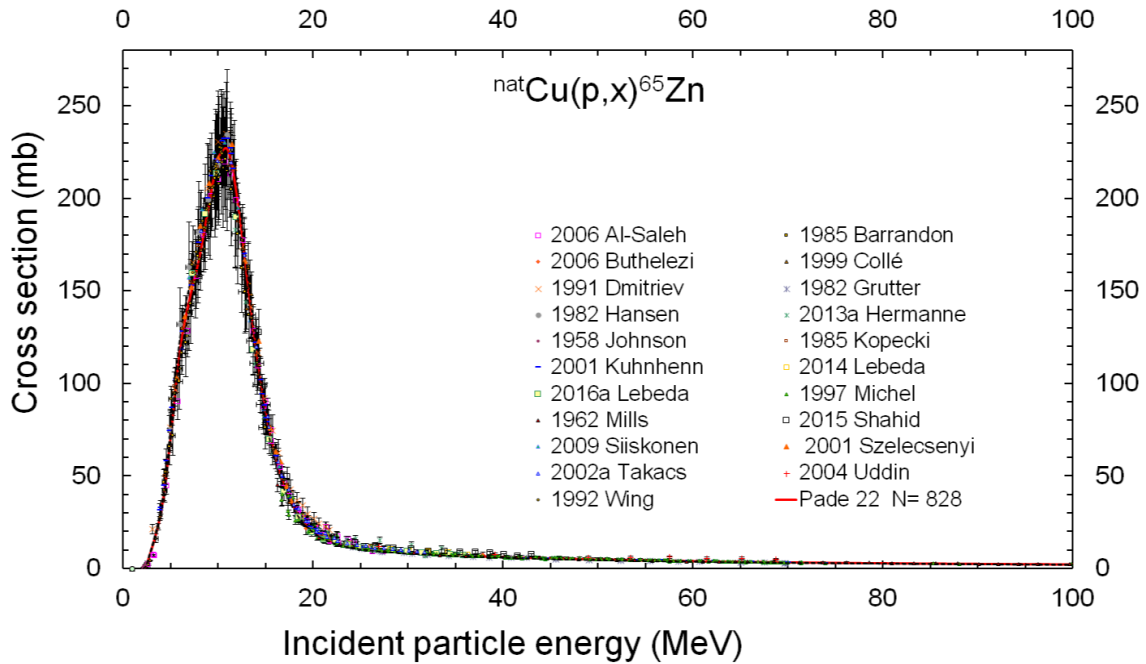
Figure 2.7. IAEA accepted cross-section data for the ^{nat}Cu(p,x)^{65}Zn reaction [3].

density of the monitor and Gd foils is well understood from precisely measuring the weight, length, width, and thickness of the foils. However, the Kapton tape used to

encase the Gd foils does not have a well characterized density due to the difficulty in accurately measuring the Si adhesive and Kapton backing.

The variance minimization technique varies the MCNP6.2 model's incident beam energy on the foil stack between 17.80 - 18.20 MeV, in .05 MeV increments. Additionally, Kapton tape and Si adhesive density are varied between 85-105% of their nominal values. Each of model's output files' were used in Equation 2.7 to obtain a model-predicted current for each monitor reaction throughout the stack. The standard deviation of these predicted monitor reaction currents and the experimentally measured currents are taken, in which the lowest value represents the beam energy and Kapton/Si density for the model. The results and further detail of this process are described in Section 2.5.2.

2.6   Previous Cross-section Measurements

Two previous measurements of the ^{160}Gd(p,n)^{160}Tb excitation function exist [9]. The first experiment was performed to obtain experimental data for a theoretical model, much like the motivation for this work. The Birattari experiment used a cyclotron to produce a proton beam, striking Gd foils consisting of natural Gd, similar to the ones used in this experiment. One initial difference between the previous and current experiment is the areal densities of each foil used. The Birattari experiment used Gd foils with an areal density of 19 mg/cm^2 (no uncertainty provided), while the foils in this experiment ranged from 6.46 - 9.51 $\pm$ 0.365 mg/cm^2 [9].

Birattari used a Faraday cup to collect charge in order to determine the proton beam current [9]. This charge was converted to proton current by dividing by the charge of a proton in Coulombs. This thesis experiment uses a different approach to determine the total proton fluence, which will be discussed in a following section.

The Birattari paper also did not utilize a stacked foil technique. The cyclotron was

able to produce a beam with an energy range between 16-45 MeV; Al degraders were used to hit energies below 16 MeV. Birattari's energy uncertainty ranged between 250 - 500 keV, while the uncertainty in this experiment ranged between 150 - 930 keV. The larger uncertainty is a function of the energy broadening as the proton beam progresses through the foil stack. However, an advantage to the stack foil technique used in this experiment is having additional experimental measurements in a given energy range. Birattari has seven data points in the 4-18 MeV energy range, while this experiment has 15.

The Birattari cross-section was determined using a single γ-decay at 879 keV. This experiment determined the cross-section of the ^{160}Gd(p,n) reaction by using the four most intense decays of ^{160}Tb, the 298, 879, 966, and 1178 keV [23]. Another difference is that in 1973, the intensity of the 879 keV γ decay was 32.1%, while today evaluated the intensity is 30.1% 6 [23].

Similar to Birattari and this experiment, Vermeulen's experiment occured using two separate cyclotrons. It is unclear from his paper which of the two the ^{160}Tb measurement was performed on. Vermeulen's Gd foils were significantly thicker towards the beginning of the stack (18.49 mg/cm^3) than the Gd foils used in this experiment; however, the Gd foils towards the back of the stack, where the relevant ^{160}Tb measurement was made, had an areal density of 6.7 mg/cm^3 (no uncertainty provided). Vermeulen utilized a stacked foil technique with Al degraders to reduce the beam energy from 66 MeV to 16 and 12 MeV, where the ^{160}Tb cross-section measurements occurred. Vermeulen used a Faraday cup at the rear of the stack, along with Cu and Ti monitor foils to determine the initial current, which were within 5% of each other. Vermeulen's ^{160}Tb cross-section measurements were determined using the 966 and 1177 keV γ-decays.

III. Methodology

This chapter utilizes the theory described in Chapter 2 to walk through the steps taken to build the MCNP6.2 and the Transport of Ions in Material (TRIM) models, design the experiment, and obtain experimental results.

3.1 MCNP Model Methodology

A MCNP6.2 model was developed to model charged particle energy loss throughout each layer of the foil stack. Runs of up to 10 million protons were performed to model the energy loss in order to determine spacing and placement of each of the Gd foils to provide data points spread approximately evenly across the 4-18 MeV energy range. The model also allowed the maximum amount of monitor foils to be placed within the stack to get additional data on proton beam energy and fluence at each Gd foil location. Without this model, there would be a risk of adding too many monitor foils, potentially stopping the beam inside the stack, resulting in redundant cross-section measurements due to poor spacing of the Gd foils.

The design of the foil stack was accomplished by modeling the measured geometry of each foil (length width, thickness, and density) in the MCNP input deck, located in Appendix A. The MCNP models used the default ENDF/B-VII.1 libraries for reaction data [15]. Any gaps in proton data libraries were filled with TENDL-2017's library [13]. While TENDL-2019 is available, at the time of modeling, it did not have the .ace files necessary to import a cross-section into MCNP. Physics models are enabled to perform charged particle transport as described in Section 2.2.

The cyclotron beam was modeled as a mono-directional point beam along the x-axis, centered at the middle of the foil stack. The beam was modeled with a Gaussian energy spread of 2% [20, 24]. The *F8:h tally was used to model the average energy

lost in each cell [15]. This gave an estimate of the mean energy for the proton beam as it passed into each of the foils in the stack. Through iteration, a foil stack was designed, which included 15 evenly-spaced Gd foils and 17 monitor foils.

Figure 3.1 shows each of the materials used and their location in the foil stack. The iron foil used at the beginning of the stack was there to provide a radiograph of the beam spread to ensure it was collimated at the center of the first Cu foil. The stainless steel foil at the end of the stack was to act as a beam stop and ensure the beam remained collimated throughout the stack. Additionally, this depiction, along with the MCNP model and the TRIM model assume all foils in close-contact with one another. However, a small gap between each foil, roughly $\frac{1}{16}$ of an inch exist. Since the foil stack is under vacuum, this "close-contact" assumption is made in all of the modeling, because there is no medium between each foil for the protons to interact with. However, this underestimates the beam spread in the model. Since neutron reaction channels do not contribute to the production of ^{160}Tb, secondary neutron analysis was not conducted.

Figure 3.1. Visualization of foils stack implemented in this work. All Gd foils were encapsulated in Kapton tape.

After the foil stack was designed, other tallies were added to the model to extract information for post-processing the data. The first was the F1:h tally which quantified the distribution of proton energies impacting each foil. This allowed the proton energy distributions to be characterized and ensure the distribution of energies, which ultimately represented the uncertainty of the cross-section measurement in energy space, were acceptable and with minimal overlap.

The final piece to the MCNP6 model was described in Section 2.5.2, where the Kapton density and the initial beam energy are iterated over using MCNP's pStudy

[25]. Beam energy is varied between 17.8 MeV - 18.2 MeV based upon variances seen in past experiments at LBNL's 88-Inch cyclotron [20, 24], and the areal density of the Kapton and Kapton adhesive varied between 0.95 - 1.05% of nominal. The result of the double iteration is 189 output files of different density and beam energy combinations that were used in a minimization routine to determine the energy and density most consistent with the measured monitor data.

3.2 TRIM Model

A TRIM model was produced to visualize the physical spread of the protons as they pass through successive foils [21]. As shown in Figure 3.2, the spread of the beam from the beginning to the end of the stack is roughly 280 μm. This is approximately 10% of the average 25,000 μm foil height.
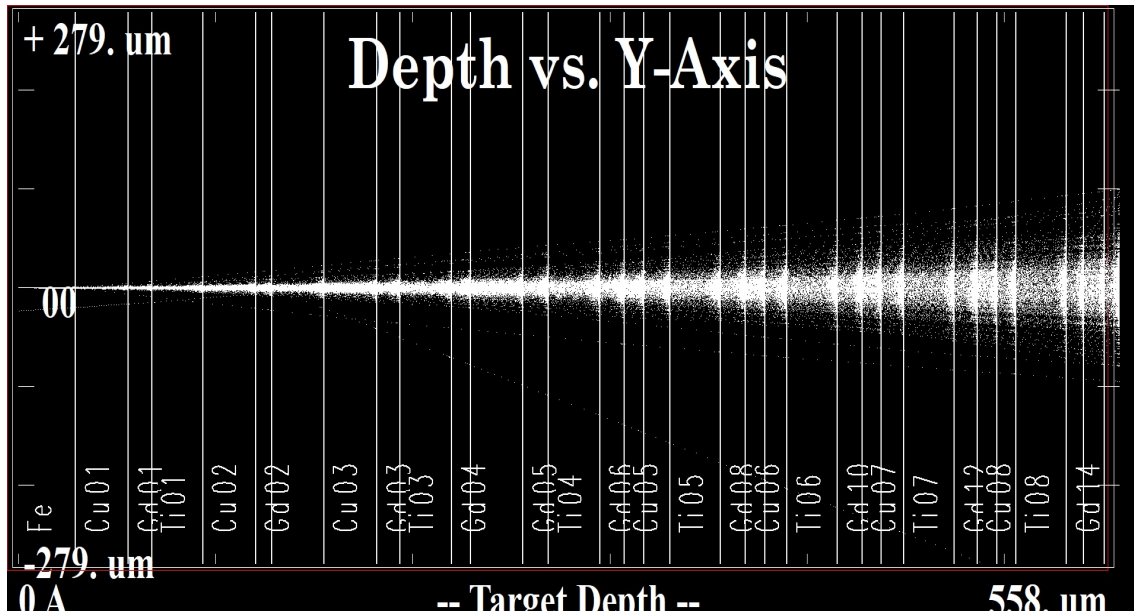

Figure 3.2. TRIM depiction of beam spread after 1000 ions incident on foil stack.

This TRIM model uses the actual measured foil thicknesses, but there are a few limitations to the TRIM model. First, the TRIM input only allows for 50 layers of material. To accommodate this requirement, the Kapton tape, which encapsulates

27

the Gd foils, is not modeled. The foils were prioritized over the Kapton due to their much larger areal density (larger by a factor of 4 through 8, depending on the foil). TRIM also models the beam as a point source, while the LBNL Cyclotron beam had a diameter of approximately 1 cm, as seen in Figure 3.3. Nonetheless, the experimentally measured beam spot results were consistent with the predicted divergence of the model, and all protons impinged on the foils as designed.
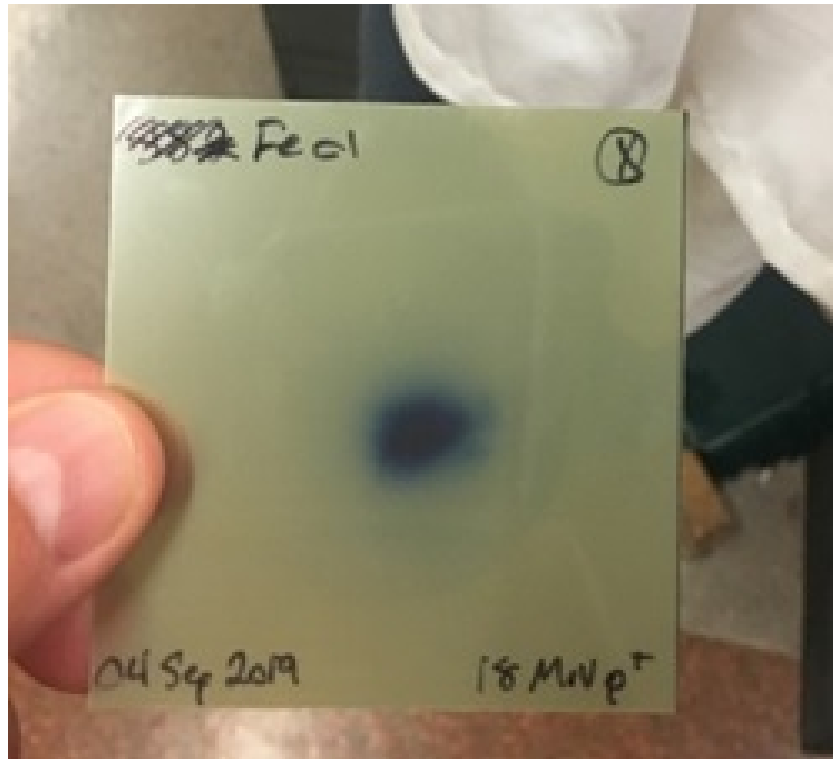

Figure 3.3. Radiograph image of the beam spot entering the foil stack.

3.3 Experimental Setup

Each reaction, monitor, and radiographic foil were manufactured by Goodfellow. They were weighed using a Mettler Toledo ME104E scale (SN:B824000042). Their length and width measured with General ULTRATECH stainless steel calipers, while their thicknesses were measured with Mitutoyo High Accuracy Digimatic Micometers

(SN:293-130-10) to precisely determine their thickness and areal density as the Good-Fellow stated uncertainty in thickness ranged from 10-25%. The results are shown in Table 3.1 for each foil in the stack.

After each foil was weighed and measured, they were mounted onto Lucite slides, depicted in Figure 3.4a. Monitor foils were mounted by taping their edges to the slide, leaving the majority of the foil exposed to the beam, shown in Figure 3.4c. Gd foils were encapsulated completely in Kapton tape, as depicted in Figure 3.4b. After mounting, all foils were placed in the foil holding apparatus depicted in Figure 3.4d.

The cyclotron beam was tuned to 18 MeV and focused to a beam spot size shown in Figure 3.3, roughly 1-cm^2. The foil stack was irradiated for 5400 secs, and HPGe counting began 12 minutes after irradiation. Each monitor foil was counted on the LBNL HPGe for the ^{nat}Ti(p,x)^{48}V, ^{nat}Ti(p,x)^{46}Sc, ^{nat}Cu(p,x)^{62}Zn, ^{nat}Cu(p,x)^{63}Zn, and ^{nat}Cu(p,x)^{65}Zn products. Data for shorter lived ^{nat}Gd(p,x) reactions were also collected. Foils were then shipped to the Air Force Institute of Technology (AFIT) for longer HPGe counting. Each Gd foil was counted for 24 hours at AFIT.

Many ^{nat}Gd(p,x) reactions were observed in the AFIT HPGe measurements, as shown in Table 3.2. For the purposes of this research, only the ^{160}Gd(p,n)^{160}Tb reaction was studied, but the methodology and framework established can be applied to the remaining data at a future date.

The ^{nat}Ti(p,x)^{48}V, ^{nat}Ti(p,x)^{46}Sc and ^{nat}Cu(p,x)^{65}Zn monitor reactions, described in Table 3.3, were also counted at AFIT. Monitor reaction data from LBNL proved inconsistent, likely due to very high detector dead times, sometimes exceeding 50%, the monitor reaction data from LBNL was not used for this analysis.

Table 3.1. Target stack measured foil specification. The foils are listed in order of interaction with the incident beam. The uncertainties are calculated from propagating each piece of measuring equipment's uncertainty.

Foil	Thickness (μm)	Areal Density (mg/cm^2)
Fe	29 ± 0.5	19.8 ± .34
Cu-01	26.9 ± 0.083	22.55 ± .42
Gd-01	11.8 ± 0.187	8.61 ± .37
Ti-01	26.2 ± 0.255	11.09 ± .21
Cu-02	26.7 ± 0.05	22.40 ± .42
Gd-02	9.0 ± 0.1	6.50 ± .37
Ti-02	26.7 ± 0.296	11.24 ± .21
Cu-03	26.9 ± 0.083	22.63 ± .42
Gd-03	11.5 ± 0.122	8.39 ± .37
Ti-03	26.4 ± 0.543	11.30 ± .21
Gd-04	9.0 ± 0.277	6.92 ± .37
Cu-04	26.6 ± 0.010	22.28 ± .42
Gd-05	12.7 ± 0.218	9.31 ± .37
Ti-04	26.1 ± 0.148	11.16 ± .21
Gd-06	12.4 ± 0.218	9.01 ± .37
Cu-05	10.6 ± 0.187	8.90 ± .42
Gd-07	13.0 ± 0.192	9.51 ± .37
Ti-05	25.8 ± 0.444	11.05 ± .21
Gd-08	12.7 ± 0.335	9.23 ± .37
Cu-06	9.9 ± 0.449	8.34 ± .42
Gd-09	11.0 ± 0.217	8.05 ± .37
Ti-06	22.6 ± 0.083	10.95 ± .21
Gd-10	12.5 ± 0.164	9.10 ± .37
Cu-07	9.7 ± 0.083	8.17 ± .42
Gd-11	11.6 ± 0.206	8.43 ± .37
Ti-07	22.6 ± 0.148	10.95 ± .21
Gd-12	11.5 ± 0.083	8.37 ± .37
Cu-08	10.1 ± 0.158	8.48 ± .42
Gd-13	9.5 ± 0.384	6.90 ± .37
Ti-08	25.6 ± 0.166	10.94 ± .21
Gd-14	8.8 ± 0.229	6.59 ± .37
Cu-09	10.6 ± 0.192	8.88 ± .42
Gd-15	10.2 ± 0.25	7.41 ± .37
SS	130 ± 0.5	104 ± 7.28
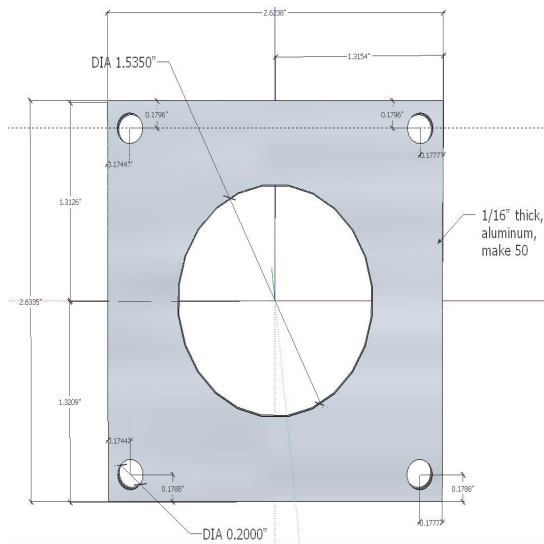
(a) **Lucite Slide Schematic**
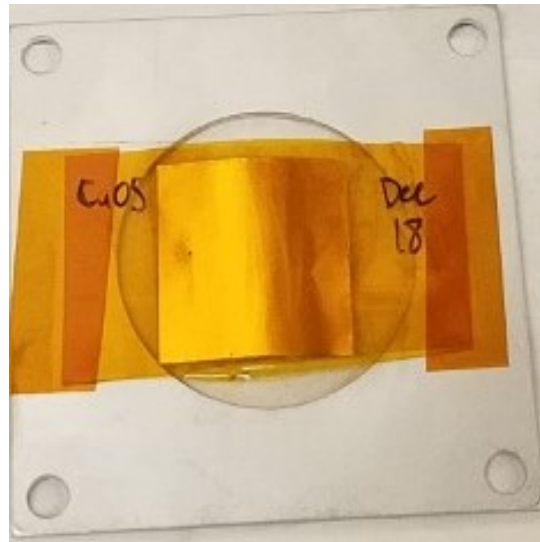
(b) **Kapton Encapsulated Foil**
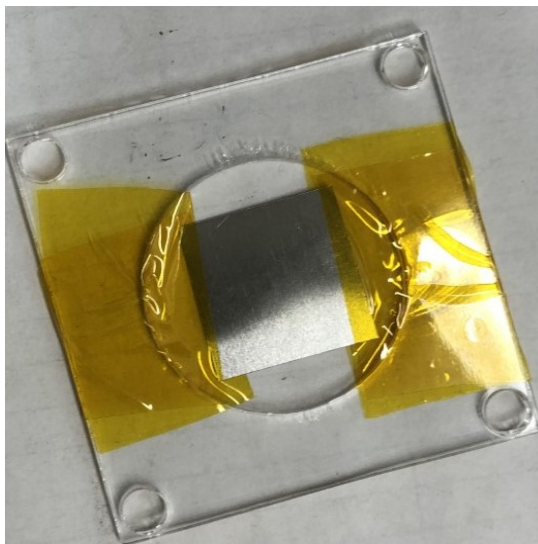
(c) **Ti Monitor Foil**
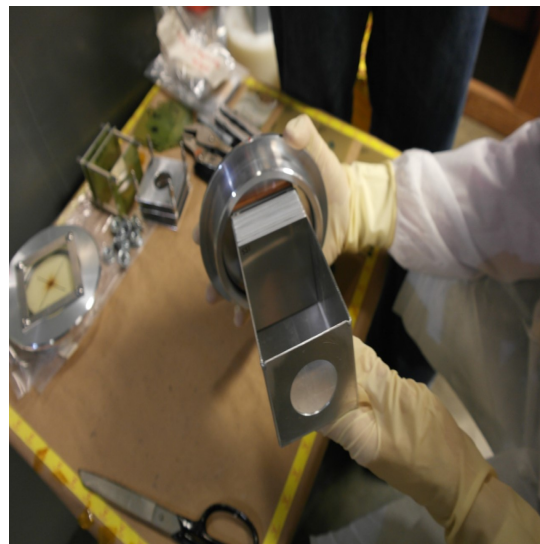
(d) **Foil Holding Apparatus**

Figure 3.4. Schematic of mounting equipment and mounting strategy for Gd and monitor foils.

3.4 Data Analysis Methodology

3.4.1 HPGe Calibration

To obtain an energy calibration on the AFIT HPGe, a multi-nuclide source, containing the isotopes shown in Appendix B was used. The AFIT HPGe has an energy

Table 3.2. Observed Gd reactions from the experimental data.

Reaction to measure	Half life of product	Gamma to Measure (keV)	Intensity(%)
^{160}Gd(p,n)^{160}Tb	72.3 days	298,879,966,1177	26.1,30.1,25.1,14.9
^{nat}Gd(p,x)^{157}Eu	15.2 hrs	410	17.8
^{nat}Gd(p,x)^{159}Gd	18.5 hrs	363	11.78
^{nat}Gd(p,x)^{154}Tb	21.5 hrs	123,1274	26, 10.5
^{154}Gd(p,2n)^{153}Tb	2.34 days	212	31.0
^{nat}Gd(p,x)^{155}Tb	5.32 days	105	25.1
^{nat}Gd(p,x)^{156}Tb	5.35 days	534	67
^{nat}Gd(p,x)^{154}Eu	8.6 years	723, 1274	20.06, 34.8
^{nat}Gd(p,x)^{152}Eu	13.5 years	344	2.4

Table 3.3. Monitor reactions used for this analysis to measure the ^{160}Gd(p,n)^{160}Tb cross section.

Reaction to measure	Half life of product	Gamma to Measure (keV)	Intensity(%)	Foils possible
^{nat}Cu(p,n)^{65}Zn	243.9 days	1115	50.04	All Cu
^{nat}Ti(p,x)^{46}Sc	83.79 days	889,1120	99.984, 99.987	Front 6 Ti
^{nat}Ti(p,x)^{48}V	15.9735 days	983, 1312	99.98, 98.2	All Ti

calibration of 0.3663 keV/channel and a 13-bit digitizer (8,192 channels) [2]. Once calibration data were collected, the primary peaks of each source were fit to their corresponding channels in PeakEasy 4.98.1 [4].

Efficiency at each of the data points from the calibration sources is given by

$$\epsilon = \frac{C}{A_t \, t_c \, BR} \tag{3.1}$$

where C represents the counts in each energy peak collected from the calibration source(s), A_t is the activity of the source [Bqs] at time of counting, t_c is the counting time [sec], and BR is the intensity of the γ-decay. However, the calculated efficiencies from the calibration sources are not at each of the decay energies associated with

the ^{160}Tb and monitor reaction products. To determine the efficiency at any energy, efficiency points from each calibration source were fitted to a HPGe efficiency function using Python's curve fit function. The HPGe efficiency function is given by

$$\epsilon = Aln(E_\gamma) + B\frac{ln(E_\gamma)}{E_\gamma} + C\frac{ln(E_\gamma)^2}{E_\gamma} + D\frac{ln(E_\gamma)^4}{E_\gamma} + E\frac{ln(E_\gamma)^5}{E_\gamma}, \qquad (3.2)$$

where A , B, C, D,and E are fit parameters and E_γ is the gamma decay energy [26]. Plotting the curve fitted optimized values for A , B, C, D,and E gives a detector efficiency curve across all relevant energies. An example energy calibration for 10 cm at AFIT is shown in Figure 3.5.
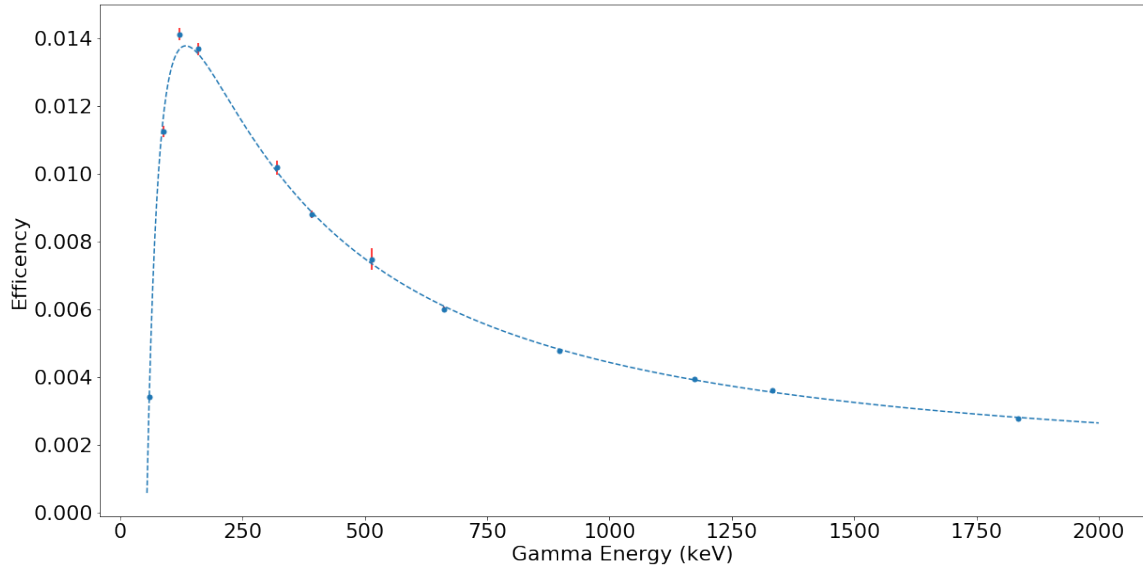

Figure 3.5. **Efficiency calibration for AFIT's HPGe at 10 cm obtained from the multi-nuclide source.**

3.4.2 Determination of Induced Activities

Using the efficiency calibration from Equation 3.2 for each detector, the T_0 activity can be calculated from

$$A_0 = \frac{C\lambda e^{\lambda t_j}}{(1 - e^{-\lambda t_c})\epsilon f_t BR}, \tag{3.3}$$

where C is the number of counts in a given peak, λ is the decay constant of the product [sec^{-1}], t_j is the amount of time between the end of irradiation and the beginning of counting [sec], t_c is the amount of counting time [sec], ϵ is the detector efficiency at the energy corresponding to C, f_t is the fraction of live time, and BR is the branching ratio of the gamma decay being measured.

PeakEasy was used to calculate the amount of counts in a given peak from the HPGe gamma spectrum. This program allows the user to draw bounds around a peak and returns a goodness-of-fit to the data based upon a Chi-squared analysis between the two. PeakEasy allows users to select single or multiple Gaussians; a linear, quadratic, or cubic background; a low-energy tail; and/or a step function to better fit the observed data. Figure 3.6 has an excerpt from PeakEasy showing the goodness of fit for an example ^{160}Tb decay.
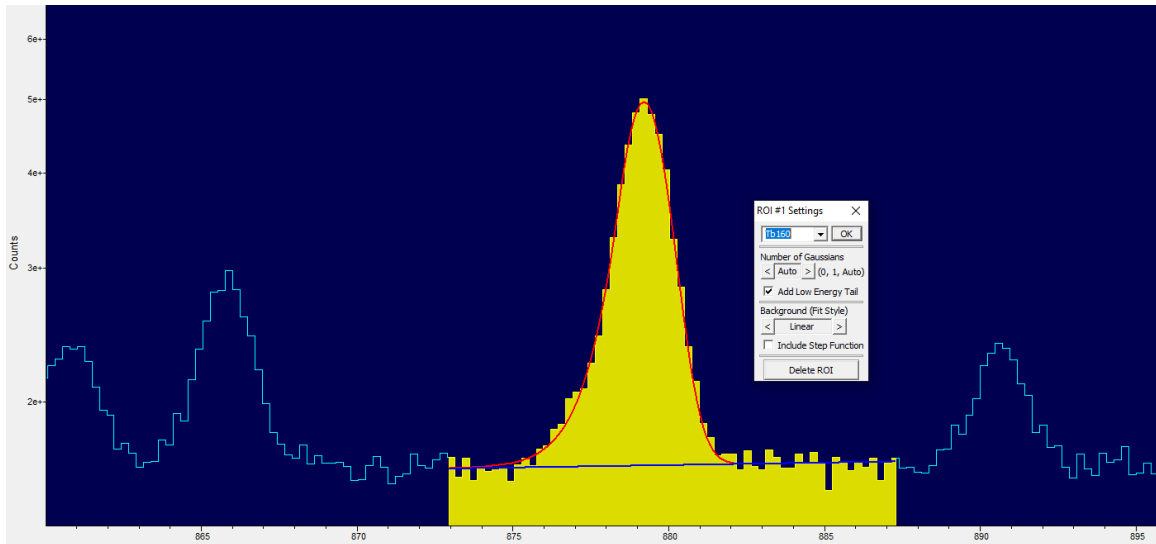

Figure 3.6. PeakEasy graphical user interface with peak fitting options shown [4].

t_j is determined by calculating the difference between the end of irradiation and the beginning of counting. The beginning of counting time is displayed in PeakEasy.

34

Information concerning the f_t, and t_c for each measurement are also displayed in PeakEasy. The λ and BR are obtained from National Nuclear Data Center [23].

3.4.3   Hot Ion Recoils

When a charged particle interacts with atoms in the foil, some of its kinetic energy is transferred to the reaction product nucleus. If this interaction occurs at the foil boundary, the recoiling nucleus can escape and deposit into the next foil. This effect was seen in the HPGe data where primary gamma decay lines for a given reaction were seen in the subsequent foil.

To illustrate how this phenomenon was accounted for, consider an example foil, Ti-01, which is placed before foil Cu-01 in the foil stack. Analyzing the data from foil Cu-01 will show ^{48}V decays resulting from hot ion recoils leaving the Ti-01 foil and depositing in Cu-01. The ^{48}V activity observed in the Cu-01 foil was added to the activity observed in the Ti-01 foil to determine the total induced activity. This was repeated for all foils. This effect was minor and primarily observed in the Ti and 10 μm Cu foils (thin and "low" Z). Overall, the result of this analysis was relatively minor and resulted in a ~1% increase in activity for each monitor foil in which this was observed.

3.4.4   Determining Proton Beam at Each Foil

To determine the flux-weighted energy for the cross-section measurements, the proton distribution was tallied in the MCNP6 model for each of the Gd foils. Results from this tally are shown in Figure 3.7.

Figure 3.7. Graph of modeled proton energy distributions in each Gd foil.

While the distributions closely follow a Gaussian distribution, there is a low energy tail resulting in a slight shift of the mean. This low energy tail is extracted and plotted

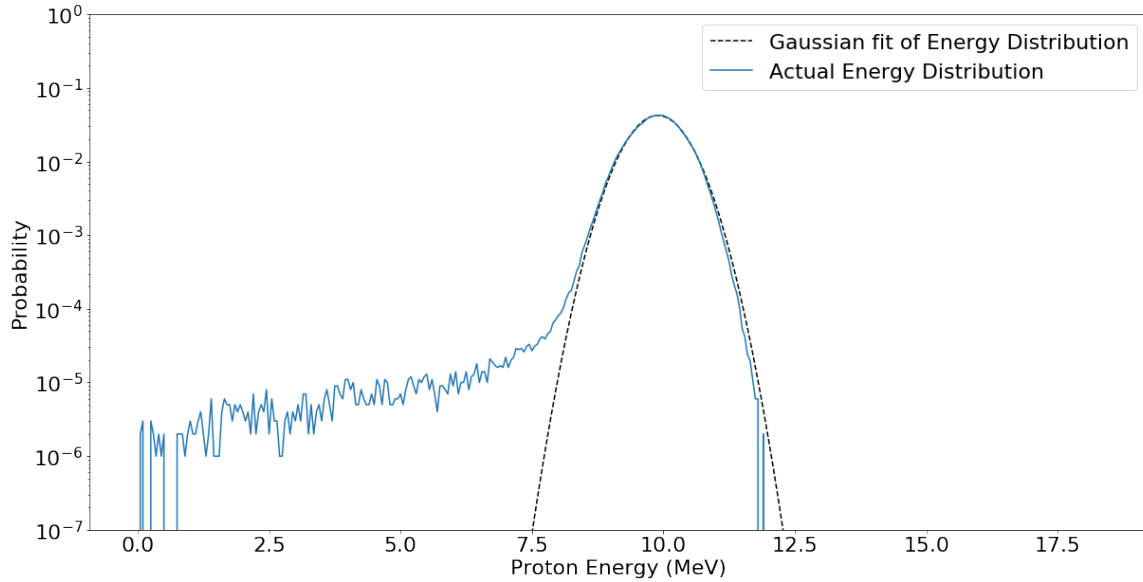against the Gaussian fit for an arbitrarily selected foil, Gd-10, in Figure 3.8

Figure 3.8. Proton energy distribution plotted with Gaussian fit for foil Gd-10.

Therefore, the mean energy was determined by a flux-weighted average as

$$\langle E \rangle = \frac{\int E \frac{d\phi}{dE} dE}{\int \frac{d\phi}{dE} dE},$$

(3.4)

where $\langle E \rangle$ is the flux-weighted proton energy in each foil, E represents the energy for each proton, and $\frac{d\phi}{dE}$ is the differential proton flux obtained from MCNP6 modeling of proton transport for a specific foil [16]. Figure 3.8 shows the difference between the flux-weighted average and the Gaussian fit for foil Gd-10. The Gaussian fit predicts a mean energy of 9.89 MeV, while the flux-weighted average predicts a mean energy of 9.87 MeV.

3.4.5   Determining Proton Fluence

Proton fluence was determined by using a weighted mean of the monitor foil currents around each Gd-foil, termed a compartment for bervity, throughout the stack. The T_0 activities from the $^{nat}Ti(p,x)^{46}Sc$, $^{nat}Ti(p,x)^{48}V$, and $^{nat}Cu(p,x)^{65}Zn$

were calculated and used in conjunction with Equation 2.7 to determine a current from each monitor reaction channel. The monitor reactions from each compartment were used to calculate an uncertainty weighted average current for each compartment. The weighting coefficients for each was the inverse of their uncertainty squared. Next, a linear fit was performed to determine the slope of the current drop along with the initial current at the beam energy predicted from variance minimization. This resulted in a 644 ± 9.1 nAh incident current.

From the monitor reaction data shown in Figure 3.9 and the initial proton fluence from Section 3.4.5, a comparison can be made between the MCNP6 modeled proton fluence degradation and the measured fluence. This enables a minimization routine to be performed to identify the density and incident proton beam energy most consistent with experimental results. For this analysis, the MCNP6 model varied the density of both the Si adhesive and the Kapton from 85% - 105 % of nominal. Likewise, cyclotron beam energy was varied between 17.80 MeV - 18.20 MeV in 0.05 increments, since a variance has been seen in previous experiments [20, 24].
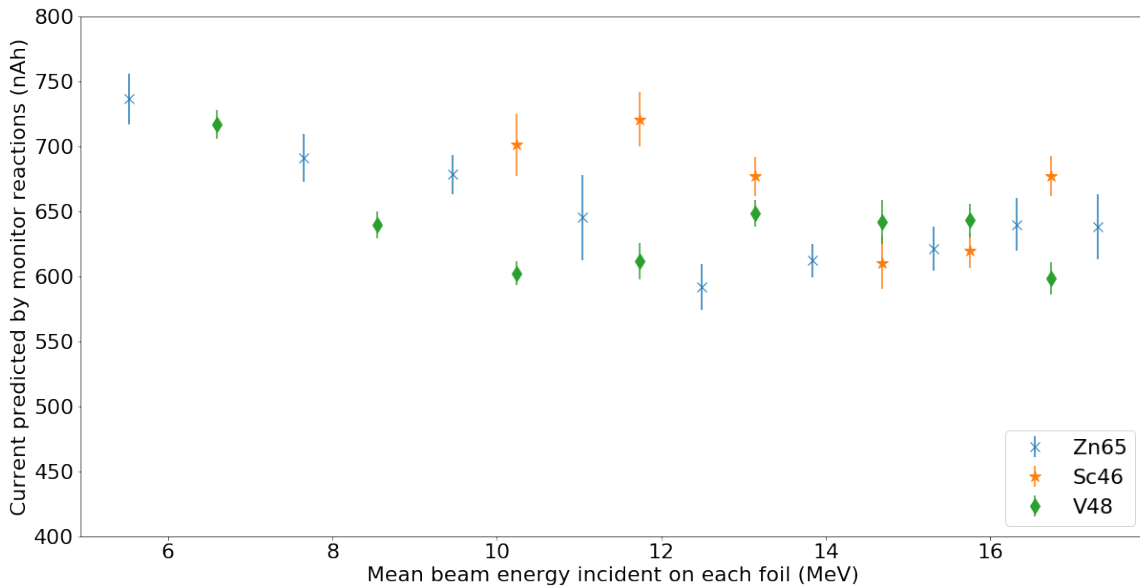

Figure 3.9. Monitor foil predicted current as a function of beam energy before variance minimization.

3.4.6   Variance Minimization of Proton Fluence

This resulted in 189 MCNP6 output files, which were read into Python and compared to the experimental results. Comparison was performed by taking the standard deviation of the three monitor reactions used, $^{nat}Cu(p,x)^{65}Zn$, $^{nat}Ti(p,x)^{48}V$, and $^{nat}Ti(p,x)^{46}Sc$ as described in Section 2.5.2. Figure 3.10 shows the results of this variance minimization, with the optimum energy being 18.05 MeV and optimum Kapton density being 95% of the nominal density. The results are consistent with previous results that have shown a small reduction in Kapton density and up to a couple hundred keV variance in nominal beam energy for the 88-Inch Cyclotron and the specific Kapton tape used [16, 20].
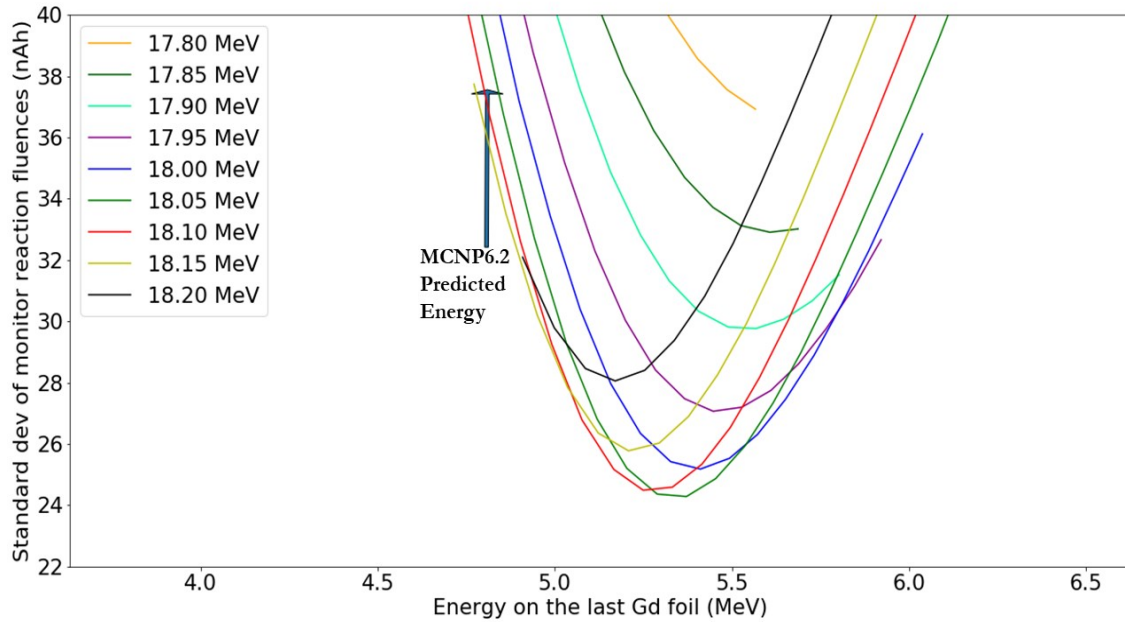
Figure 3.10. Results from variance minimization as a function of average proton energy in the Gd-15 showing that an incident beam energy of 18.05 MeV was most consistent with the measured monitor data.

Figure 3.11 show the results of the variance minimization on the current indicated by the monitor reactions throughout the foil stack. After variance minimization, there is an overall reduction in the current variance throughout the stack as seen

when comparing Figure 3.11 with Figure 3.9. Additionally, while Figure 3.9 showed an increase in current toward the rear of the stack, which is non-physical. Figure 3.11 shows a decrease in current, which is expected.
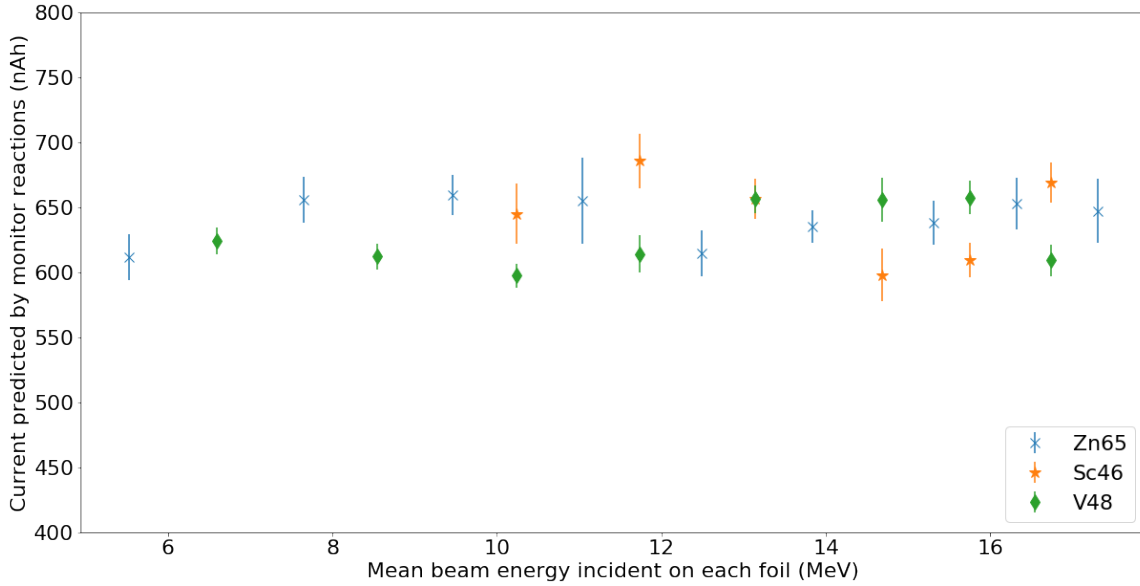

Figure 3.11. Final proton fluences throughout the target stack determined from the variance-minimized monitor reaction observed fluence.

The initial predicted beam current, using the front-most monitor reactions was 633.4 ± 8.9 nAh, where the post-variance minimization beam current was 644.0 ± 9.1 nAh. The updated current originates from the results shown in Figure 3.12, where a curve fit of the weighted mean monitor reactions is used to predicted the current incident onto the beam stack at 18.05 MeV. Using this combination of density and incident beam energy, the proton fluence drop was modeled by a linear fit to the measured uncertainty-weighted compartment currents. This data shows a 3.7% drop in current from the Gd-01 to Gd-15. This drop, in comparison with the monitor reaction mean proton fluences are shown in Figure 3.12. This ultimately adjusts the measured cross-section values later in the stack by accounting for the lower current at each position in the foil stack. Utilizing a charge collector, such as a Faraday Cup, does not account for this current drop throughout the foil stack.
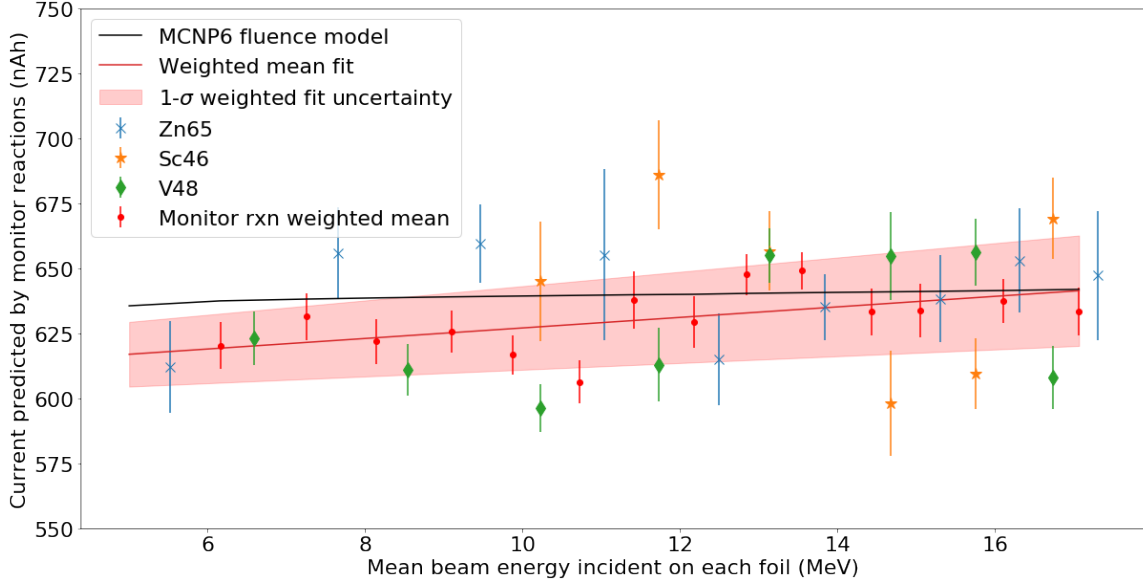
Figure 3.12. **Final mean proton fluences throughout the target stack, based on the variance-minimized observed fluence from the $^{nat}Cu(p,x)^{65}Zn$, $^{nat}Ti(p,x)^{46}Sc$, and $^{nat}Ti(p,x)^{48}V$ monitor reactions. The fluence drops by approximately 3.7% from the incident fluence of 644 ± 21 nAh.**

Figure 3.12 also shows the MCNP modeled results in comparison with the experimental results. MCNP predicts a 1% reduction in current throughout the stack, significantly less than the measured 3.7%. The drop in current is due to two different proton interaction mechanisms: nuclear reactions and angular scattering. For the nuclear reactions mechanism, there is a dearth of data underpinning the evaluated cross-sections used in this stack, hence the reason for this research. Several reaction channels relied on the built-in MCNP models, which have shown to under-predict reaction rates in previous research. Other reaction channels utilized the TENDL cross-section data, which has varying degress of accuracy and experimental validation. Therefore, it is not surprising that the MCNP model would under-predict the current drop throughout the stack, and it is not used for determining the current in this work.

3.4.7 Cross Section Calculation

The cross section can be calculated from A_0, Equation 3.3, as

$$\sigma = \frac{A_0}{I \frac{\rho N_a}{AW} t_{foil}(1 - e^{-\lambda t_i}) f_{iso}},$$ (3.5)

where A_0 is the T_0 activity [Bqs], I is the beam current in units of $\frac{protons}{sec}$, ρ is the density [g/cm^3], N_a is Avogadro's Number, AW is atomic weight, t_{foil} is the thickness of a given foil [cm], t_i is the irradiation time [sec], f_{iso} is the percent of a given isotope that occurs naturally. I was determined using the methods outlined in Sections 3.4.5 and 3.4.6. ρ and t_{foil} are calculated from measured dimensions and are shown in Table 3.1.

3.5 Error Propagation

The proton energy distribution was quantified using the MCNP6 model as described in Section 3.4.4. Data from this tally, shown in Figure 3.7 was read into a Python script that extracted the proton energy distributions. The distribution in each foil was fit with a Gaussian. The standard deviation determined from the Gaussian fit is the uncertainty in energy space. While there is a slight deviation from the proton energy distribution due to the low energy tailing, this method of energy uncertainty is common in the literature [16, 18, 20, 24].

In Equation 3.1, there is uncertainty in the counts, activity, branching ratio, and counting time. While these uncertainties exists and are quantifiable, they do not represent the uncertainty in efficiency for a given [160]Tb gamma decay being measured. Rather the uncertainties in Equation 3.1 represent the uncertainty in energy at each of the decays contained in the calibration sources, which are inputs into the Python curve fitting function.

The outputs of the Python's curve fit function are the optimized variables of the function, Equation 3.2, along with a covariance matrix describing the uncertainty of the optimized values. This covariance matrix is used as an input in Python's multivariate sampling function (MVF). The MVF is used to sample 10,000 different iterations of A,B,C,D, and E from Equation 3.2, each bounded by the covariance matrix. This produces 10,000 different efficiency values at each energy peak of interest. Fitting a Gaussian to a probability distribution of these efficiencies, the sigma can be extracted to quantify the efficiency uncertainty. Figure 3.13 shows an example Gaussian fit to the ^{48}V decay at 944 keV at 19 cm.
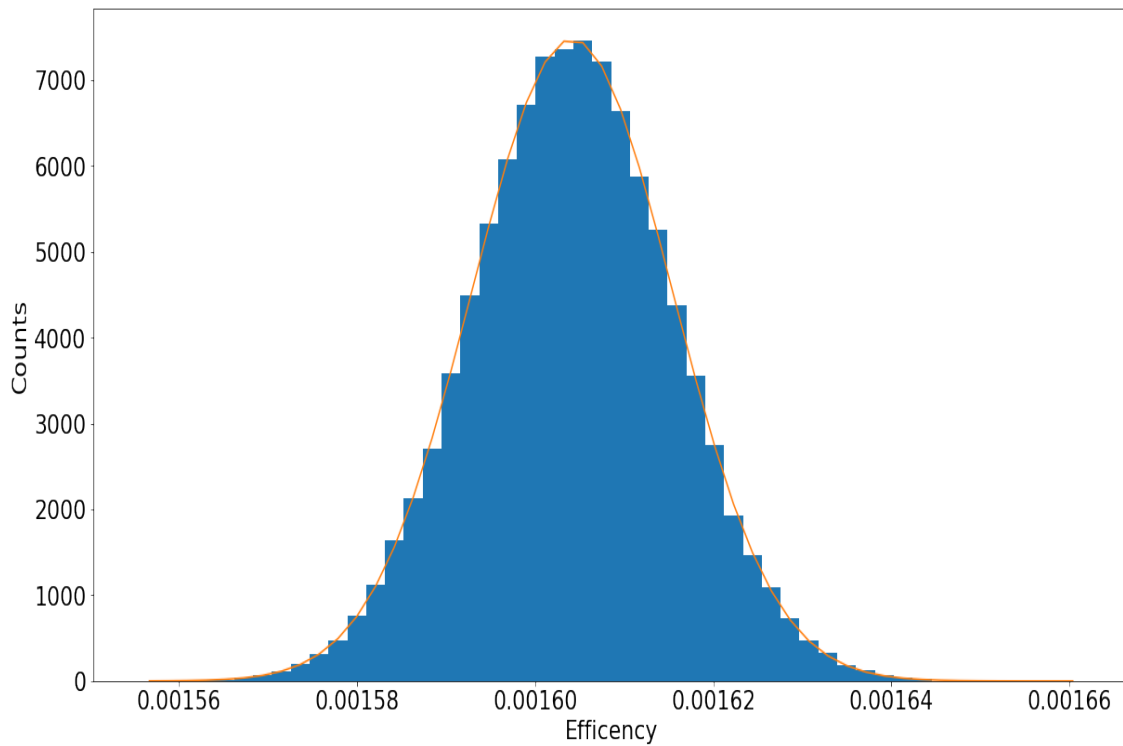

Figure 3.13. Efficiency distribution at 1115 keV for ^{65}Zn's decay on AFIT's detector at 19 cm above the HPGe crystal.

Next, other uncertainties in Equation 3.3 must be quantified. The complete uncertainty in A_0 is given as

$$\delta A_0 = A_0 \sqrt{(\frac{\delta\epsilon}{\epsilon})^2 + (\frac{\delta\lambda}{\lambda})^2 + (\frac{\delta C}{C})^2 + (\frac{\delta BR}{BR})^2 + (t_j\Delta\lambda)^2 + (t_c\Delta\lambda)^2}. \qquad (3.6)$$

The uncertainty in counts, δC, is given from the PeakEasy fitting described above [4]. The decay constant uncertainty and branching ratio uncertainty, $\delta\lambda$ and δBR, are obtained from NNDC's database [23]. The uncertainty in the time between the end of irradiation and the beginning of counting, δt_j, is known to the sec for the end of irradiation and to the sec for beginning of counting. The uncertainty in the counting time, δt_j is .5 sec, as PeakEasy tracks this to the sec [4]. The uncertainty in the fraction of live time is neglected, due to being accounted for in the δt_c.

Next, the uncertainty in the cross-section measurement is given as

$$\delta\sigma = \sqrt{(\frac{\delta A_0}{A_0})^2 + (\frac{\delta t_{Gd}}{t_{Gd}})^2 + (\frac{\delta\rho}{\rho})^2 + (t_i\Delta\lambda)^2 + (\frac{\delta I}{I})^2}. \qquad (3.7)$$

The uncertainty of the thickness of each Gd foil, δt_{Gd} is quantified by taking the standard deviation of multiple measurements taken on each foil. Similarly, the uncertainty in density $\delta\rho$ was obtained by taking the quadrature sum of of the uncertainty in length, width, mass, and thickness. Uncertainty in irradiation time, δt_i, is known to the sec. Lastly, the uncertainty in beam current, δI, is taken from the uncertainty in the linear fit to the uncertainty-weighted average at each gadolinium position.

IV. Results and Analysis

This chapter utilizes the methodology described in Chapter 3 to determine the cross-section of the ^{160}Gd(p,n)^{160}Tb reaction. In Section 4.1, the results of the efficiency curve fits are shown. In Section 4.2, the results of the A_0 calculations are shown. Finally, Section 4.3 shows the cross-section graphs compared to the previous experimental measurement, PADF and TENDL-2019 [9, 10, 13, 14].

4.1 Efficiency Results

Table 4.1 shows the efficiency values obtained using the curve fitting and bootstrapping method outlined in Section 3.4.1 and 3.5 for each reaction and monitor decay channel considered in this work. Efficiency uncertainty is relatively interesting, as this is difficult to quantify and typically neglected or taken as an assumed value. Utilizing multivariate sampling of the curve fit covariance allows for a more accurate efficiency uncertainty to be determined. However, two common constant assumed uncertainties, 0.7% and 1.0%, are decent assumptions as averages and bounding uncertainties, respectively.

Table 4.1. Isotopes, their distance from the detector, energies, and efficiencies used in determining A_0.

Rx Product	Measured Distance (cm)	Energy Level (keV)	Efficiency	Efficiency Uncertainty (%)
^{160}Gd	10	298	0.01049	0.867
^{160}Gd	10	879	0.00489	0.674
^{160}Gd	10	966	0.00454	0.694
^{160}Gd	10	1178	0.00390	0.712
^{48}V	19	983, 1312	0.00177,0.00141	0.691, 0.858
^{46}Sc	19	889, 1112	0.00191 0.00161	0.668, 0.704
^{65}Zn	19	1115	0.00160	0.708

4.2   Time-zero Activity Measurements

Table 4.2 shows the associated T_0 activities, calculated from Equation 3.3, for each isotope and foil considered in this work. When considering the ^{65}Zn activities, it is important to note that Cu-01 – Cu-04 foils are roughly 2.5x thicker than Cu-05 – Cu-08. The ^{46}Sc is significantly less active than the ^{48}V created from irradiation, which is expected with the relative magnitudes of their cross sections in this energy range. Hot ion recoils also account for an increase to the T_0 activity for ^{48}V and ^{65}Zn, which accounted for an approximately 1% increase in T_0 activity for these foils. No recoils were observed for the gadolinium foils due to the Kapton tape encasing and relatively high Z of the gadolinium limiting their overall range.

Table 4.2. A_0 for each reaction channel and foil used in this work.

Foil	Isotope Used	T_0 Activity (Bqs)	Foil	Isotope Used	T_0 Activity (kBqs)
Ti-01	^{48}V, ^{46}Sc	173.7±1.9, 0.55±0.01	Cu-09	^{65}Zn	4.38±0.05
Ti-02	^{48}V, ^{46}Sc	226.1±2.0, 0.45±0.01	Gd-01	^{160}Tb	0.38±0.01
Ti-03	^{48}V, ^{46}Sc	295.8±3.0, 0.36±0.01	Gd-02	^{160}Tb	0.29±0.01
Ti-04	^{48}V, ^{46}Sc	370.0±3.1, 0.28±0.01	Gd-03	^{160}Tb	0.40±0.01
Ti-05	^{48}V, ^{46}Sc	369.4±3.1, 0.21±0.01	Gd-04	^{160}Tb	0.31±0.01
Ti-06	^{48}V, ^{46}Sc	355.1±3.0, 0.12±0.01	Gd-05	^{160}Tb	0.50±0.01
Ti-07	^{48}V	321.2±2.7	Gd-06	^{160}Tb	0.50±0.01
Ti-08	^{48}V	189.6±1.9	Gd-07	^{160}Tb	0.60±0.01
Cu-01	^{65}Zn	3.84±0.05	Gd-08	^{160}Tb	0.71±0.02
Cu-02	^{65}Zn	5.15±0.06	Gd-09	^{160}Tb	0.75±0.02
Cu-03	^{65}Zn	7.00±0.07	Gd-10	^{160}Tb	1.01±0.02
Cu-04	^{65}Zn	10.97±0.10	Gd-11	^{160}Tb	1.08±0.02
Cu-05	^{65}Zn	6.51±0.06	Gd-12	^{160}Tb	1.21±0.03
Cu-06	^{65}Zn	8.33±0.08	Gd-13	^{160}Tb	0.75±0.02
Cu-07	^{65}Zn	8.10±0.08	Gd-14	^{160}Tb	0.28±0.01
Cu-08	^{65}Zn	6.61±0.07	Gd-15	^{160}Tb	0.10±0.01

4.3   Cross-section Measurements

Equation 3.5 was used to calculate the total cross section from the gadolinium T_0 activities shown in Table 4.2. The results are shown in Figure 4.1 for the ^{160}Gd(p,n)^{160}Tb reaction. The cross sections from this work are compared against

the TENDL-2019 and PADF evaluations. The experimental cross sections shown in Figure 4.1 are for each of the four prominent γ decay lines for ^{160}Tb decay. Each of these measurements are generally within one standard deviation of each other, and no systematic trends are observed in the relative magnitudes for each. This provides an improvement over Birattari's previous measurements where only one line, 879 keV, was used, as the branching ratio has changed from 32.1% in 1973 to 30.1% today. Additionally, Vermeulen's measurement only used two of the four γ decays, the 966 and 1177 keV, versus the four used here.

Table 4.3 shows the 15 measured experimental cross sections and the associated energy for each. The energy uncertainty represents the one-sigma uncertainty from a Gaussian fit of the proton distribution in each foil obtained from the MCNP simulations after the variance minimization. Cross-section uncertainty will be discussed below, but largely falls in the 5% range. This leads to a visual artifact in Figure 4.1 and 4.2 of practically zero error for the lower magnitude cross-sections occurring at the high and lower energy ranges. However, relative error in these ranges is not significantly different than relative error elsewhere in the foil stack.

The relative error from each of the variable terms contributing to cross-section uncertainty are shown in Table 4.4. The constant terms of uncertainty include irradiation time (0.00017%), density (3.56%), beam current (1.13 - 1.75%), efficiency (0.67 - 0.87%), decay constant (0.27%), branching ratio (1.99 - 2.30%), time between end of irradiation and beginning of counting (0.05 - 0.10%), and counting time (0.002 - 0.008%). Uncertainty in Avogadro's number, atomic weight, and mass fraction were neglected.

An uncertainty-weighted average was used to obtain a single ^{160}Gd(p,n) cross section, Figure 4.2, from the four cross-section measurements shown in Figure 4.1. These are compared to previous cross-section measurements by Birattari and Vermeulen,
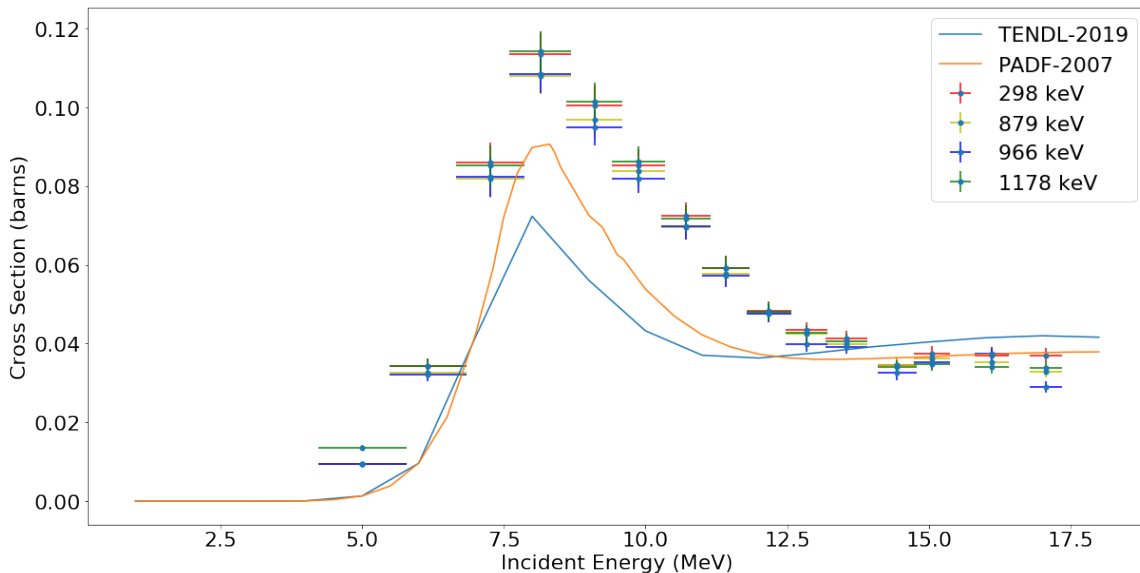
Figure 4.1. ^{160}Gd(p,n) cross-section determined for each using the four primary γ decays, compared to TENDL-2019 and PADF [13, 14].
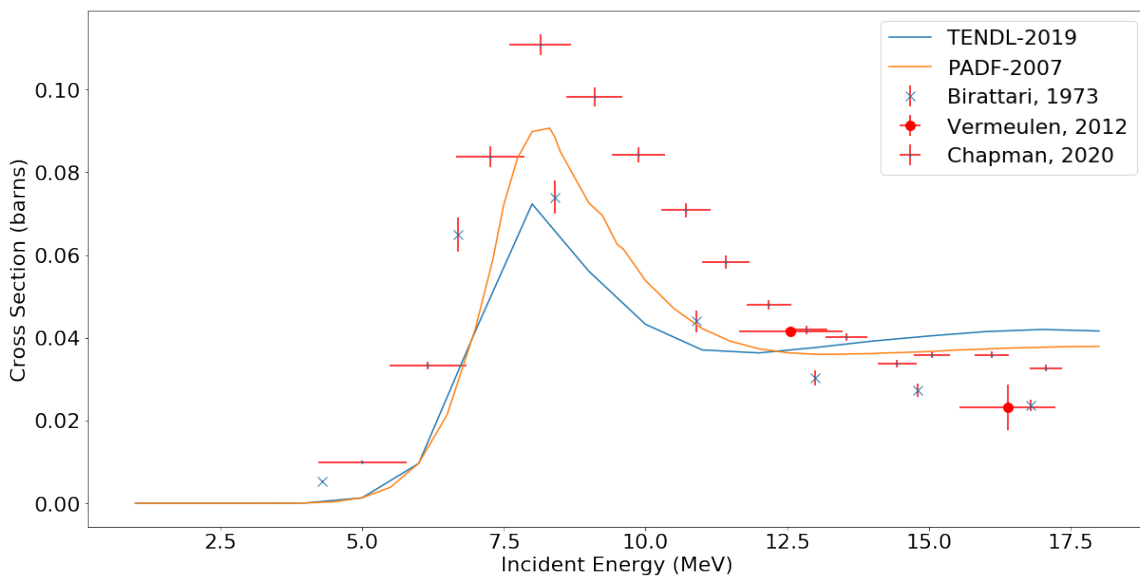

Figure 4.2. ^{160}Gd(p,n) cross-section determined by averaging the four cross-section measurements compared to PADF, TENDL-2019, and previous experimental data from Birattari and Vermeulen [9, 10, 13, 14].

along with TENDL-2019 and PADF evaluated data [9, 10, 13, 14]. The threshold behavior below ∼7 MeV closely follows the magnitude and shape measured by Birattari; both measurements indicate a higher cross-section, by approximately a factor of two, than the TENDL and PADF evaluations in this region. However, these results show a larger and broader peak cross-section than predicted by TENDL-2019, PADF-2007, and Birattari. At high energies, above ∼13 MeV, the current results are consistent with the TENDL-2019 and PADF-2007 evaluations and show an increased cross section and more gradual drop off than previous experimental results indicate.

Table 4.3. Cross sections of the ^{160}Gd(p,n)^{160}Tb reaction calculated in this work.

Foil	Energy (MeV)	Cross Section (mb)
Gd-01	17.07 ± 0.28	32.76 ± 0.95
Gd-02	16.11 ± 0.30	35.93 ± 1.00
Gd-03	15.06 ± 0.32	35.96 ± 0.98
Gd-04	14.44 ± 0.34	33.91 ± 1.03
Gd-05	13.55 ± 0.36	40.26 ± 1.10
Gd-06	12.84 ± 0.37	42.06 ± 1.15
Gd-07	12.18 ± 0.40	48.09 ± 1.27
Gd-08	11.41 ± 0.42	58.38 ± 1.66
Gd-09	10.72 ± 0.44	70.98 ± 1.90
Gd-10	9.87 ± 0.47	84.39 ± 2.15
Gd-11	9.10 ± 0.50	98.43 ± 2.56
Gd-12	8.15 ± 0.55	111.11 ± 2.72
Gd-13	7.26 ± 0.60	83.93 ± 2.64
Gd-14	6.16 ± 0.68	33.41 ± 0.91
Gd-15	5.01 ± 0.78	10.00 ± 0.28

Table 4.4. Cross section and contributing term relative percent uncertainties.

Foil	σ	A_0	Δr	C
Gd-01	2.47	2.53	1.59	1.16
Gd-02	2.37	2.53	1.21	1.17
Gd-03	2.37	2.45	1.06	0.98
Gd-04	2.72	2.50	2.92	1.10
Gd-05	2.37	2.37	1.71	0.78
Gd-06	2.40	2.36	1.76	0.76
Gd-07	2.37	2.31	1.47	0.61
Gd-08	2.65	2.27	2.65	0.45
Gd-09	2.42	2.27	1.96	0.43
Gd-10	2.29	2.25	1.31	0.32
Gd-11	2.38	2.25	1.78	0.34
Gd-12	2.25	2.25	0.72	0.36
Gd-13	3.02	2.27	4.06	0.45
Gd-14	2.62	2.37	2.61	0.78
Gd-15	2.71	2.34	2.46	0.70

V. Conclusions

5.1 Summary

This thesis experiment measured the ^{160}Gd(p,n)^{160}Tb excitation function. It showed that there is a higher peak cross-section than previously measured experimentally or calculated in the TENDL-2019 or PADF-2007 evaluations. This research can lead to optimized production of ^{160}Tb for surrogate debris by taking advantage of the peak cross-section. Additionally, this research provides additional charged particle data that can help improve reaction modeling codes by further constraining free parameters.

Previous research demonstrated stacked foil activation techniques to be efficient methods to measure excitation functions from charged particle irradiations. To develop the foil stack, a MCNP6 model was developed. This model was used to predict the distribution of proton energies interacting with each foil in the stack. From the model, a thickness and placement of the monitor and reaction foils in the stack was obtained such that the 15 reaction foils were evenly spaced in energy space. Concurrently, a TRIM model was used to analyze the physical spread of the protons passing though the foil stack to ensure that the angular spread did not exceed the foil dimensions.

Each foil's length, width, thickness, and mass were measured to quantify the areal density. Each gadolinium foil was encapsulated in Kapton tape to prevent oxidation and loss of material. The foil stack was then assembled and irradiated for 90-min with a total current of 646 nAH. After irradiation, measurements were taken of each foil with two different, calibrated HPGe detectors to determine the induced T_0 activity. Monitor foil reactions were used to verify the model and correct for beam current drop throughout the stack. Additionally, monitor foils were used in combination with

the MCNP6.2 predicited particle distributions to perform a variance minimization to determine an accurate Kapton density and beam energy. This resulted in a minimum at 18.05 MeV incident beam energy and 95% nominal densities for the Kapton backing and silicon adhesive.

The current determined in the variance minimization, along with the measured T_0 activities, were used to calculate the cross section for the ^{160}Gd(p,n)^{160}Tb reaction. The variance minimization found a 1.0% drop in current from the first Gd foil to the last. The previous experimental measurement, while not using a foil stack method, used aluminum degraders to achieve low energy measurements. The current drop that occurs when the proton beam passes through these degraders, along with the resulting spread in the energy distribution, was not captured in the previous measurement.

These cross-section measurements are slightly higher than Birattari's previous experimental measurements and Vermeulen's higher energy measurement. However, these measurements agree with the lower energy measurement from Vermeulen. Aside from the current drop discussed above, another main reason for the cross-section increase is the change in branching ratio from 1973 to 2020. In 1973, the γ-decay used to measure this cross-section had a decay intensity of 32.1% [9]. Today, the reported intensity is 30.1% [11]. Equation 3.3 has BR in the denominator, meaning the modern-day lower BR corresponds to higher T_0, which then corresponds to a 6.2% higher σ according to Equation 3.5. Additionally the cross-sections determined here are a weighted mean of four different γ-decays, meaning if there are significant changes to the BR in the future, it is less likely to impact these results.

5.2 Future Work

The gadolinium foils used in this stack were natural gadolinium, which contains seven different isotopes(^{152}Gd ^{154}Gd, ^{155}Gd, ^{156}Gd, ^{157}Gd, ^{158}Gd, and ^{160}Gd). Which

only the ^{154}Gd(p,n)^{154}Tb and the ^{156}Gd(p,α)^{153}Eu reactions have experimental measurements [11].

Table 3.2 shows the potential reactions that are energetically possible based upon an 18 MeV proton beam entering the foil stack. Quick, 5-min collections of each Gd foil was performed on the LBNL HPGe detector within hours of irradiation to capture these short-lived isotopes in addition to longer 24 hour counts at AFIT. Future analysis of the HPGe detector data from this experiment can be performed to make several, first-ever measurements of some of the nuclear reactions listed in Table 3.2. These reactions are of value to improve the existing nuclear data in order to further inform and constrain nuclear reaction models.

Additionally, another experiment using the same or similar foil stack without encapsulating the Gd foils in Kapton tape would be of interest. The tape was obviously accounted for in the modeling, and through variance minimization, but it would be interesting to see how the cross-section measurement would be without it entirely. This would also allow for a quantification of oxidation over time, as the HPGe measurements could be repeated at later dates to determine how the T_0 activity changes as a function of time and as oxidation takes effect.

Appendix A. GitHub Repository

The simulation input files and Python codes for this research described above are provided in a private online repository on **GitHub**. For access to this repository, please contact the author. Specific items of interest in this repository are extracted below:

- **MCNP model**: This is the model that contains each of the foil's geometry, along with the actual densities of each foil, and the NDS experimental cross-sections for monitor reactions in order to obtain accurate beam energy degradation throughout the stack.

- **Python Code**: This jupyter notebook contains all of the code needed to produce the figures found in the thesis. It contains functions to translate HPGe detector data and convert it to cross-section measurements by implementing the equations found in the thesis.

- **Experimental Data**: This is a folder containing all of the monitor and Gd foil measurements taken from the HPGe detectors at AFIT and LBNL.

Eckert & Ziegler

Isotope Products

24937 Avenue Tibbitts
Valencia, California 91355

Tel 661·309·1010
Fax 661·257·8303

CERTIFICATE OF CALIBRATION
MULTINUCLIDE STANDARD SOURCE

Customer:	AIR FORCE INSTITUTE OF TECHNOLOGY	**Source No.:**	2087-1-1
P.O. No.:	EN19DEN357-MC	**Reference Date:**	1-Jun-19 12:00 PST
Catalog No.:	GF-ML	**Contained Radioactivity:**	1.011 μCi 37.41 kBq

Physical Description:

- A. Capsule type: D (25.4 mm OD x 6.35 mm maximum THK)
- B. Nature of active deposit: Evaporated metallic salts
- C. Active diameter/volume: 5 mm
- D. Backing: Epoxy
- E. Cover: Acrylic

Mult 2087-1-1 May 19

Gamma-Ray Energy (keV)	Nuclide	Half-life	Branching Ratio (%)	Activity (μCi)	Gammas per second	Total Uncert.
60	Am-241	432.17 ± 0.66 years	36.0	0.03045	405.6	3.1 %
88	Cd-109	462.6 ± 0.7 days	3.63	0.2732	366.9	3.1 %
122	Co-57	271.79 ± 0.09 days	85.6	0.01133	358.8	3.1 %
159	Te-123m	119.7 ± 0.1 days	84.0	0.01583	492.0	3.1 %
320	Cr-51	27.706 ± 0.007 days	9.86	0.3559	1298	3.0 %
392	Sn-113	115.09 ± 0.04 days	64.9	0.05095	1223	3.0 %
514	Sr-85	64.849 ± 0.004 days	98.4	0.06443	2346	3.0 %
662	Cs-137	30.17 ± 0.16 years	85.1	0.04590	1445	3.0 %
898	Y-88	106.630 ± 0.025 days	94.0	0.1077	3746	3.0 %
1173	Co-60	5.272 ± 0.001 years	99.86	0.05508	2035	3.0 %
1333	Co-60	5.272 ± 0.001 years	99.98	0.05508	2038	3.0 %
1836	Y-88	106.630 ± 0.025 days	99.4	0.1077	3961	3.0 %

Method of Calibration:

This source was prepared from weighed aliquots of solutions whose concentrations in μCi/g were determined by gamma spectrometry.

Notes:

- See reverse side for leak test(s) performed on this source.
- EZIP participates in a NIST measurement assurance program to establish and maintain implicit traceability for a number of nuclides, based on the blind assay (and later NIST certification) of Standard Reference Materials (as in NRC Regulatory Guide 4.15).
- Nuclear data was taken from IAEA-TECDOC-619, 1991.
- Overall uncertainty is calculated at the 99% confidence level.
- This source has a recommended working life of 1 year.

Daniel James Van Dalsem
    Quality Control

27-May-19
    Date

EZIP Ref. No.:   2087-1

──── ISO 9001 CERTIFIED ────

Medical Imaging Laboratory
24937 Avenue Tibbitts   Valencia, California 91355

Industrial Gauging Laboratory
1800 North Keystone Street   Burbank, California 91504

Bibliography

1. K. Zieb, H. G. Hughes, M. R. James, and X. G. Xu, "Review of heavy charged particle transport in MCNP6.2," *Nuclear Instruments and Methods in Physics Research, Section A: Accelerators, Spectrometers, Detectors and Associated Equipment*, vol. 886, no. January, pp. 77–87, 2018.

2. G. F. Knoll, *Radiation Detection and Measurement, Third Edition.* John Wiley & Sons, Inc., 2000. [Online]. Available: https://books.google.com/books/about/Radiation{_}Detection{_}and{_} Measurement.html?id=HKBVAAAAMAAJ{&}pgis=1

3. A. Hermanne, A. V. Ignatyuk, R. Capote, B. V. Carlson, J. W. Engle, M. A. Kellett, T. Kibédi, G. Kim, F. G. Kondev, M. Hussain, O. Lebeda, A. Luca, Y. Nagai, H. Naik, A. L. Nichols, F. M. Nortier, S. V. Suryanarayana, S. Takács, F. T. Tárkányi, and M. Verpelli, "Reference Cross Sections for Charged-particle Monitor Reactions," *Nuclear Data Sheets*, vol. 148, pp. 338–382, 2018.

4. B. Rooney and P. Felsher, "PeakEasy," 2018. [Online]. Available: https://peakeasy.lanl.gov/

5. NSAC Isotopes Subcommittee, "Meeting Isotope Needs and Capturing Opportunities for the Future: The 2015 Long Range Plan for the DOE-NP Program," Tech. Rep., 2015.

6. F. Kondev, M. Thoennessen, J. Batchelder, T. Kawano, J. Kelley, E. McCutchan, M. Smith, A. Sonzogni, and I. Thompson, "White Paper on Nuclear Data Needs and Capabilities for Basic Science," Tech. Rep., 2017. [Online]. Available: https://arxiv.org/ftp/arxiv/papers/1705/1705.04637.pdf

7. L. Bernstein, C. Romano, D. A. Brown, R. Casperson, M.-a. Descalle, M. Devlin, and C. Pickett, "Final Report for the Workshop for Applied Nuclear Data Activities," pp. 1–53, 2019.

8. D. R. Nethaway, "Fission split and the ^{161}Tb Soil Correction," 1991.

9. C. Birattari, E. Gad, E. GADIOLI ERBA tt, A. M. Grassi Strini, G. Strini, and G. Tagliaferri, "Not to be reproduced by photoprint or microfilm without written permission from the publisher PRE-EQUILIBRIUM PROCESSES IN (p,n) REACTIONS," *Nuclear Physics A*, vol. 201, pp. 579–592, 1973. [Online]. Available: https://ac-els-cdn-com. afit.idm.oclc.org/0375947473903229/1-s2.0-0375947473903229-main.pdf? {_}tid=17219995-a6a6-4044-b2de-c1832396eda8{&}acdnat=1555419793{_} deb6a68d3761fe7aa7f4ed9133c989d4

10. C. Vermeulen, G. F. Steyn, F. Szelecsényi, Z. Kovács, K. Suzuki, K. Nagatsu, T. Fukumura, A. Hohn, and T. N. Van Der Walt, "Cross sections of proton-induced reactions on natGd with special emphasis on the production possibilities of 152Tb and 155Tb," *Nuclear Instruments and Methods in Physics Research, Section B: Beam Interactions with Materials and Atoms*, vol. 275, pp. 24–32, 2012. [Online]. Available: http://dx.doi.org/10.1016/j.nimb.2011.12.064

11. B. Pritychenko, "The Experimental Nuclear Reaction Data (EXFOR): Extended Computer Database and Web Retrieval System," *Nuclear Instruments and Methods in Physics Research Section A: Accelerators, Spectrometers, Detectors and Associated Equipment*, vol. 888, 2018.

12. "TALYS," 2019. [Online]. Available: https://tendl.web.psi.ch/tendl{_}2019/talys.html

13. "TALYS-based evaluated nuclear data library." [Online]. Available: https://tendl.web.psi.ch/tendl{_}2019/tendl2019.html

14. C. H. M. Broeders, U. Fischer, A. Y. K. Ã, L. Mercatali, and S. P. Simakov, "Proton Activation Data File to Study Activation and Transmutation of Materials Irradiated with Protons at Energies up to 150 MeV," *Nuclear Science and Technology*, vol. 44, no. 7, pp. 933–937, 2007.

15. J. Armstrong, F. B. Brown, J. S. Bull, L. Casswell, L. J. Cox, D. Dixon, R. A. Forster, J. T. Goorley, H. G. Hughes, J. Favorite, R. Martz, C. C. J. Solomon, and A. Zukaitis, "User's Manual Code Version 6.2," 2018.

16. A. S. Voyles, L. A. Bernstein, E. R. Birnbaum, J. W. Engle, S. A. Graves, T. Kawano, A. M. Lewis, and F. M. Nortier, "Excitation functions for (p,x) reactions of niobium in the energy range of E p = 40-90 MeV," *Nuclear Instruments and Methods in Physical Research B: Beam Interactions with Materials and Atoms*, vol. 429, pp. 1–34, 2018. [Online]. Available: https://arxiv.org/pdf/1804.06548.pdf

17. U. S. Customs, B. Protection, D. Nuclear, and D. Office, "Compendium of Material Composition Data for Radiation Transport Modeling," 2011. [Online]. Available: www.pnnl.gov/main/publications/external/technical{_}reports/pnnl-15870rev1.pdf

18. S. A. Graves, P. A. Ellison, T. E. Barnhart, H. F. Valdovinos, E. R. Birnbaum, F. M. Nortier, R. J. Nickles, and J. W. Engle, "Nuclear excitation functions of proton-induced reactions (E p = 35-90 MeV) from Fe, Cu, and Al," *Nuclear Instruments and Methods in Physical Research B: Beam Interactions with Materials and Atoms*, vol. 386, 2016. [Online]. Available: http://dx.doi.org/10.1016/j.nimb.2016.09.018

19. Department of Energy, "Nuclear Data Needs and Capabilities for Applications," Tech. Rep., 2015. [Online]. Available: https://www.faa.gov/data{_}research/aviation/aerospace{_}forecasts/media/FY2017-37{_}FAA{_}Aerospace{_}Forecast.pdf

20. J. T. Morrell, A. S. Voyles, M. S. Basunia, J. C. Batchelder, E. F. Matthews, and L. A. Bernstein, "Measurement of ^{139}La(p,x) Cross Sections from 35-60 MeV by Stacked-Target Activation," *The European Physical Journal A*, pp. 1–14, 2019. [Online]. Available: http://arxiv.org/abs/1907.04431

21. J. F. Ziegler, J. P. Biersack, and M. D. Ziegler, *SRIM - The Stopping and Range of Ions in Matter*, 2015.

22. K. S. Krane, *Introductory Nuclear Physics*. Corvallis, OR: John Wiley & Sons, 1988.

23. "NuDat 2.7." [Online]. Available: https://www.nndc.bnl.gov/

24. A. S. Voyles, A. M. Lewis, J. T. Morrell, M. S. Basunia, L. A. Bernstein, J. W. Engle, S. A. Graves, and E. F. Matthews, "Proton-induced reactions on Fe, Cu, & Ti from threshold to 55 MeV," *ArXiv*, pp. 1–25, 2019. [Online]. Available: http://arxiv.org/abs/1910.11135

25. F. B. Brown, J. E. Sweezy, and R. Hayes, "Monte Carlo parameter studies and uncertainty analyses with MCNP5," *Proceedings of the PHYSOR 2004: The Physics of Fuel Cycles and Advanced Nuclear Systems - Global Developments*, pp. 121–129, 2004.

26. Z. Kis, B. Fazekas, J. Östör, Z. Révay, T. Belgya, G. L. Molnár, and L. Koltay, "Comparison of efficiency functions for Ge gamma-ray detectors in a wide energy range," *Nuclear Instruments and Methods in Physics Research, Section A: Accelerators, Spectrometers, Detectors and Associated Equipment*, vol. 418, no. 2-3, pp. 374–386, 1998.

REPORT DOCUMENTATION PAGE

Form Approved
OMB No. 0704–0188

1. REPORT DATE *(DD–MM–YYYY)*	2. REPORT TYPE	3. DATES COVERED *(From — To)*
03–02–2020	Master's Thesis	May 2018 - March 2020

4. TITLE AND SUBTITLE

Measurement of the ^{160}Gd(p,n)^{160}Tb excitation function from 4-18 MeV using a stacked foil technique

5a. CONTRACT NUMBER

5b. GRANT NUMBER

5c. PROGRAM ELEMENT NUMBER

6. AUTHOR(S)

Chapman, Ryan K., Major, USAF

5d. PROJECT NUMBER

5e. TASK NUMBER

5f. WORK UNIT NUMBER

7. PERFORMING ORGANIZATION NAME(S) AND ADDRESS(ES)

Air Force Institute of Technology
Graduate School of Engineering and Management (AFIT/EN)
2950 Hobson Way
WPAFB OH 45433-7765

8. PERFORMING ORGANIZATION REPORT NUMBER

AFIT-ENP-MS-20-M-088

9. SPONSORING / MONITORING AGENCY NAME(S) AND ADDRESS(ES)

Air Force Technical Applications Center
AFTAC
POC: MAJ Brett Castle (brett.castle@us.af.mil)
1211 S Patrick Dr.
Patrick AFB, FL 32925

10. SPONSOR/MONITOR'S ACRONYM(S)

AFTAC

11. SPONSOR/MONITOR'S REPORT NUMBER(S)

12. DISTRIBUTION / AVAILABILITY STATEMENT

Distribution Statement A. Approved for public release; Distribution Unlimited.

13. SUPPLEMENTARY NOTES

This material is declared work of the U.S. Government and is not subject to copyright protection in the United States.

14. ABSTRACT

A stack of thin Gd, Ti, and Cu foils were irradiated with an 18 MeV proton beam at Lawrence-Berkeley National Laboratory's 88-Inch Cyclotron to investigate the ^{160}Gd(p,n)^{160}Tb nuclear reaction for nuclear forensics applications. This experiment will improve knowledge of ^{160}Tb production rates, allowing ^{160}Tb to be efficiently created in a foil stack consisting of other proton induced isotopes for forensics applications. A set of 15 measured cross sections between 4-18 MeV for ^{160}Gd(p,n)^{160}Tb were obtained using a stacked foil technique. The foil stack consisted of one stainless steel, one iron, fifteen gadolinium, nine copper, and eight titanium foils. The stainless steel and iron foils were used to radiograph the beam spot size. Each Gd foil was encapsulated in Kapton tape prior to irradiation to minimize oxidation. The copper, ^{62}Cu(p,n)^{62}Zn and ^{65}Cu(p,n)^{65}Zn, and titanium, ^{48}Ti(p,n)^{48}V and ^{nat}Ti(p,x)^{46}Sc, foils served as monitor foils to determine the proton fluence throughout the stack. Variance minimization using a MCNP6.2 model was used to improve the reliability of the cross-section measurements by reducing the uncertainties in proton energy and fluence by varying the density and incident beam energy within the uncertainty in the measurement of each. The measured cross section of the ^{160}Gd(p,n)^{160}Tb generally follows the shape predicted by TENDL-2019, but the cross sections obtained in this work indicate approximately a 20% increase in the maximum cross section. Additionally, other ^{nat}Gd(p,x) reactions were created through the irradiation, providing experimental measurements of ^{154}Gd(p,2n)^{153}Tb, ^{155}Gd(p,α)^{152}Eu, ^{155}Gd(p,2n)^{154}Tb, ^{155}Gd(p,n)^{155}Tb, ^{156Gd}(p,n)^{156}Tb, ^{157}Gd(p,α)^{154}Eu, ^{160}Gd(p,α)^{157}Eu, and ^{160}Gd(p,d)^{159}Gd reactions.

15. SUBJECT TERMS

Nuclear Data, Stacked Foil Technique, Cross-section measurement

16. SECURITY CLASSIFICATION OF:

a. REPORT	b. ABSTRACT	c. THIS PAGE
U	U	U

17. LIMITATION OF ABSTRACT

UU

18. NUMBER OF PAGES

70

19a. NAME OF RESPONSIBLE PERSON
Major James E. Bevins, AFIT/ENP

19b. TELEPHONE NUMBER *(include area code)*
(937)255-3636 x.4767; james.bevins@afit.edu

Standard Form 298 (Rev. 8–98)
Prescribed by ANSI Std. Z39.18